

1 Global Terrestrial Water Storage and Drought Severity under Climate Change

2
3 Yadu Pokhrel^{1*}, Farshid Felfelani¹, Yusuke Satoh², Julien Boulange², Peter Burek³, Anne
4 Gädeke⁴, Dieter Gerten^{4,5}, Simon N. Gosling⁶, Manolis Grillakis⁷, Lukas Gudmundsson⁸, Naota
5 Hanasaki², Hyungjun Kim⁹, Aristeidis Koutroulis⁷, Junguo Liu¹⁰, Lamprini Papadimitriou¹¹,
6 Jacob Schewe⁴, Hannes Müller Schmied^{12,13}, Tobias Stacke¹⁴, Camelia-Eliza Telteu¹², Wim
7 Thiery^{15,8}, Ted Veldkamp^{16,17}, Fang Zhao^{18,4} and Yoshihide Wada^{3,17}

8
9 ¹Department of Civil and Environmental Engineering, Michigan State University, East Lansing,
10 MI, USA

11 ²National Institute for Environmental Studies, Tsukuba, Japan

12 ³International Institute for Applied Systems Analysis, Laxenburg, Austria

13 ⁴Potsdam Institute for Climate Impact Research (PIK), Member of the Leibniz Association,
14 Potsdam, Germany

15 ⁵Humboldt-Universität zu Berlin, Berlin, Germany

16 ⁶School of Geography, University of Nottingham, Nottingham, UK

17 ⁷School of Environmental Engineering, Technical University of Crete, Chania, Greece

18 ⁸Institute for Atmospheric and Climate Science, ETH Zurich, Zurich, Switzerland

19 ⁹Institute of Industrial Science, the University of Tokyo, Tokyo, Japan

20 ¹⁰School of Environmental Science and Engineering, Southern University of Science and
21 Technology, Shenzhen, China

22 ¹¹Cranfield Water Science Institute (CWSI), Cranfield University, Cranfield, Bedfordshire, UK

23 ¹²Institute of Physical Geography, Goethe-University Frankfurt, Frankfurt am Main, Germany

24 ¹³Senckenberg Leibniz Biodiversity and Climate Research Centre Frankfurt (SBiK-F), Frankfurt
25 am Main, Germany

26 ¹⁴Institute of Coastal Research, Helmholtz-Zentrum Geesthacht (HZG),
27 Geesthacht, Germany

28 ¹⁵Department of Hydrology and Hydraulic Engineering, Vrije Universiteit Brussel, Brussels,
29 Belgium

30 ¹⁶Department of Water & Climate Risk, VU University, Amsterdam, the Netherlands

31 ¹⁷Department of Physical Geography, Utrecht University, Utrecht, Netherlands

32 ¹⁸Department of Geographic Sciences, East China Normal University, Shanghai, China

33
34 *e-mail: ypokhrel@egr.msu.edu
35

36 **Abstract**

37 Terrestrial water storage (TWS) strongly modulates the hydrological cycle and is a key
38 determinant of water availability and an indicator of drought. While historical TWS variations
39 have been studied, future changes in TWS and the linkages to droughts remain unexamined.
40 Here, using ensemble hydrological simulations, we show that climate change could reduce TWS
41 in many regions, especially in the southern hemisphere. A strong inter-ensemble agreement
42 indicates high confidence in the projected changes that are driven primarily by climate forcing,
43 rather than land-water management activities. Declines in TWS translate to increase in future
44 droughts. By the late-21st century global land area and population in extreme-to-exceptional
45 TWS drought could more than double, each increasing from 3% during 1976-2005 to 7% and 8%,
46 respectively. Our findings highlight the importance of climate change mitigation to avoid
47 adverse impacts on TWS and related droughts, and the need for adaptation to improve water
48 resource management.

49
50

51 TWS—the sum of continental water stored in canopies, snow and ice, rivers, lakes and
52 reservoirs, wetlands, soil, and groundwater—is a critical component of the global water and
53 energy budget. It plays key roles in determining water resource availability¹ and modulating
54 water flux interactions among various Earth system components². Further, observed changes in
55 TWS are inherently linked to droughts²⁻⁶, floods⁷, and global sea level change⁸⁻¹¹. Despite such
56 importance, global TWS remains less studied relative to hydrological fluxes (e.g., river
57 discharge, evapotranspiration, and groundwater flow) owing to the lack of large-scale
58 observations and challenges in explicitly resolving all TWS components in hydrological
59 modeling¹². This generally holds true for historical analyses; crucially, no study has to date
60 examined the potential impacts of future climate change on global TWS.

61

62 Recent modeling advancements¹³ have improved the representation of TWS in global
63 hydrological models^{14,15} (GHMs) and land surface models¹² (LSMs). The Gravity Recovery and
64 Climate Experiment (GRACE) satellite mission provided added opportunities to improve and
65 validate TWS simulations in these models. GRACE TWS data and model simulations, often in
66 combination, have been used for wide ranging applications including the assessment of water
67 resources and impacts of human activities on the water cycle^{14,16}, quantifying aquifer
68 depletion^{12,14,17-19}, monitoring drought^{3-6,20}, and assessing flood potential⁷. These studies have
69 advanced the understanding of global TWS systems that are continually changing under natural
70 hydro-climatic variability and accelerating human land-water management activities, but the
71 focus has been on historical variabilities in TWS. Further, future projections from general
72 circulation models (GCMs) have been used to quantify climate change impacts on hydrological
73 fluxes²¹⁻²³ and storages, but the projections of storages are limited to a subset of TWS
74 components—specifically soil moisture and snow²⁴⁻²⁶—owing to an incomplete representation of
75 TWS components in the GCMs. The lack of explicit parameterizations for surface water and
76 groundwater processes and the use of shallow rooting depth in GCMs has particularly hindered
77 comprehensive TWS projections using GCM simulations²⁵.

78

79 Because TWS represents total water availability on land, it also provides an integrated measure
80 of overall drought condition in a region^{5,6}. Drought—a slow-evolving climate phenomenon—is
81 among the costliest natural disasters²⁷ that directly affects water resources, agriculture, socio-

82 economic development, and ecosystem health, and is often linked with armed conflicts²⁸. A rich
83 body of literature exists on the study of droughts using indices such as the standardized
84 precipitation index (SPI²⁹), Palmer drought severity index (PDSI³⁰), soil moisture drought index
85 (SMI^{31,32}), and standardized runoff index (SRI³³). These conventional indices have been used in
86 monitoring and projecting^{32,34} meteorological, agricultural, and hydrological droughts³⁵.
87 Recently, a new drought index, the TWS drought severity index (TWS-DSI⁵), has been
88 employed to examine droughts^{36,37} in relation to the vertically-integrated water storage as
89 opposed to the individual storages or fluxes used in conventional indices. Previous studies^{5,36,37}
90 have demonstrated that TWS-DSI correlates with the conventional indices in regions with long-
91 term water storage change, but provides an integrated measure, especially by capturing the
92 effects of slow-responding terms (i.e., deep soil moisture and groundwater). Further, an
93 increasing number of TWS-based drought studies have shown that a synergistic combination of
94 TWS and traditional drought indices can provide crucial insights about drought impacts on
95 hydrologic systems and vegetation growth^{6,36,37}, because TWS directly responds to changes in
96 precipitation, integrates soil moisture, and modulates runoff generation, hence encompassing the
97 three aforementioned drought types³⁶. However, since previous TWS studies have focused on
98 historical droughts^{3-6,20}, the changes in future droughts due to TWS change and variability
99 remain unexamined.

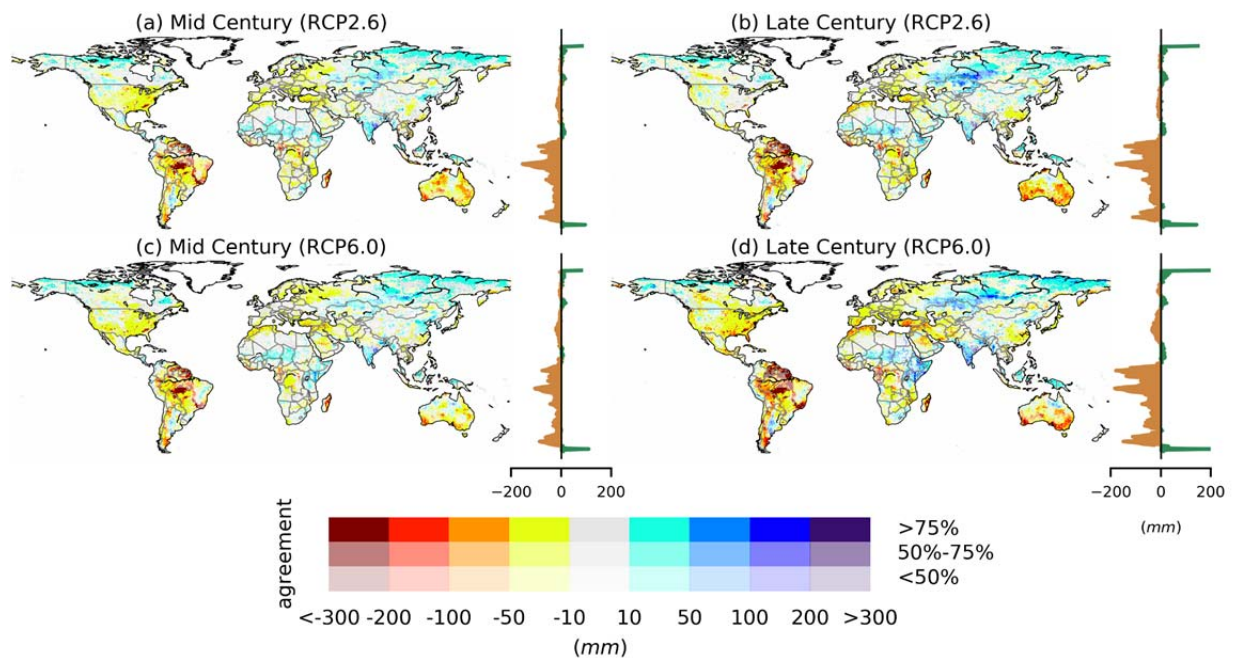
100
101 Here we present the first global assessment of the impacts of future climate change on TWS. We
102 then examine the changes in drought severity and frequency resulting from climate-induced
103 TWS change and variability by using the monthly TWS-DSI⁵ (see Methods and Supplementary
104 Table 1). We use multi-model hydrological simulations (27 ensemble members; Supplementary
105 Table 2) from seven terrestrial hydrology models (LSMs and GHMs; Supplementary Table 3)
106 driven by atmospheric forcing from four GCMs (see Methods). Four cases of radiative forcing
107 are considered for each GCM: the pre-industrial control (PIC), historical climate (HIST), and the
108 low (Representative Concentration Pathway; RCP2.6) and medium-high (RCP6.0) greenhouse
109 gas concentration scenarios (see Methods). Simulations are conducted under the framework of
110 the Inter-Sectoral Impact Model Intercomparison Project, phase 2b (ISIMIP2b³⁸;
111 <https://www.isimip.org/>). We use multi-model weighted mean of TWS anomalies, calculated by
112 weighting the ensemble members based on their continent-level skill and independence scores³⁹
113 (Methods; Extended Data Figs. 1 and 2).

115 **TWS under climate change**

116 By the mid (2030-2059) and late (2070-2099) 21st century, TWS is projected to substantially
117 decline in the majority of the southern hemisphere, the conterminous U.S., most of Europe, and
118 the Mediterranean, but increase in eastern Africa, south Asia, and northern high latitudes,
119 especially northern Asia (Fig. 1). The latitudinal mean (Fig. 1) indicates a larger decline in TWS
120 in the southern hemisphere than in the north, driven primarily by the decline in South America
121 and Australia; this is in line with the projected precipitation changes (Extended Data Fig. 3) and
122 could partly be due to a tendency of GCMs to overestimate²⁷ drying trends in the southern
123 hemisphere. The changes are evident by the mid-21st century (under both RCPs; Figs. 1a and c)
124 but the signal becomes stronger by the late-21st century, especially under RCP6.0 (Fig. 1d).
125 Exceptions are parts of the conterminous U.S. where TWS under RCP2.6 is projected to decline
126 by the mid-century but then slightly increases during the late-century, due to the projected
127 increase in precipitation across most of the region (Extended Data Fig. 3) combined with a

128 decrease in temperature from the mid- to the late-century (Extended Data Fig. 4). For RCP6.0,
 129 the projected changes (positive or negative) seen in the mid-century become more pronounced in
 130 the late-century for most global regions. The differences between the two RCPs are, however,
 131 less obvious for both periods; an exception is Australia where the spatial extent of decline in
 132 TWS is projected to be smaller under RCP6.0 than under RCP2.6 (Fig. 1), which aligns with
 133 wetter conditions projected in RCP6.0 (Extended Data Fig. 3). Globally, TWS declines
 134 (increases) in 67% (33%) of land area (excluding Greenland, Antarctica, and glaciers) by the
 135 late-21st century under RCP6.0.

136
 137
 138



139
 140 **Fig. 1 | Impact of climate change on TWS.** Shown are the changes (multi-model weighted mean) in
 141 TWS, averaged for the mid (2030-2059; a and c) and late (2070-2099; b and d) 21st century under RCP
 142 2.6 (a and b) and RCP 6.0 (c and d) relative to the average for the historical baseline period (1976-2005).
 143 Color hues show the magnitude of change and saturation indicates the agreement, among ensemble
 144 members, in the sign of change. The graph on the right of each panel shows the latitudinal mean.

145
 146 Overall, a strong agreement is found across ensemble members in the sign of change (color
 147 saturation in Fig. 1), indicating high confidence in the projections. For the late-21st century, an
 148 agreement of >50% can be seen in regions where large decline or increase in TWS is projected;
 149 such agreement is >75% for regions such as the Amazon basin, southern Australia, the
 150 Mediterranean, and eastern U.S. (Fig. 1). This confidence is reinforced by the good agreement
 151 between the simulated TWS and GRACE data for the historical period (Extended Data Fig. 5 and
 152 Supplementary Figs. 1-2). The broad global spatial patterns and seasonal variations in TWS are
 153 accurately captured by the multi-model ensemble mean, although some differences are evident in
 154 the magnitude of seasonal amplitude (Extended Data Fig. 5). Such differences stand out
 155 especially along major river channels (e.g., the Amazon, Nile, and Mississippi) that are explicitly
 156 considered in the models but not resolved in the GRACE data. Further, the seasonal dynamics

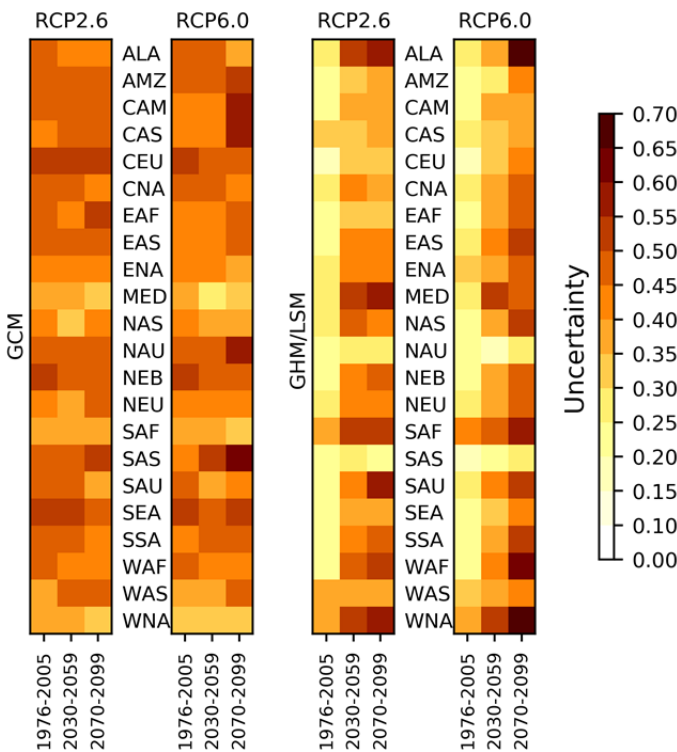
157 and inter-annual variability in the simulated TWS averaged over the major global river basins
 158 also agree reasonably well with the GRACE data (Supplementary Figs. 1-2), even though there
 159 are some disagreements between the trend in GRACE and multi-model mean (Supplementary
 160 Fig. 2), likely due to uncertainties in model parameterizations and potential biases in GCM-based
 161 forcing data.

162

163 **Uncertainty in TWS simulations**

164 The inter-ensemble spread in TWS simulations is a combination of the uncertainties arising from
 165 climate forcing (i.e., GCM) and GHM/LSM parameterizations (see Methods). The GCM
 166 uncertainty (for a given RCP scenario) is larger than GHM/LSM uncertainty in most regions for
 167 the historical period and mid-21st century (Fig. 2). However, the GHM/LSM uncertainty
 168 increases substantially with time, leading to a higher GHM/LSM uncertainty in most regions at
 169 the end of the 21st century, especially under RCP6.0. The GHM/LSM uncertainty range (Fig. 2,
 170 two right panels) for the historical period is relatively small, consistent with good agreement of
 171 the seasonal amplitude and temporal variability of TWS with GRACE data (Extended Data Fig.
 172 5 and Supplementary Figs. 1-2), which likely reflects the relative benefits of bias correction
 173 using observations for the same period.

174



175 **Fig. 2 | Uncertainty in TWS simulations.** Shown are contributions of GCMs and GHMs/LSMs to the
 176 uncertainty in TWS simulations (the range statistic of quantile-based TWS index; see Methods), averaged
 177 over the sub-continental regions defined by the Intergovernmental Panel on Climate Change (IPCC)
 178 Special Report On Extremes (SREX; region description is provided in Supplementary Fig. 3). The
 179 horizontal axis denotes historical baseline period (1976-2005) and mid (2030-2059) and late (2070-2099)
 180 21st century. A lighter color marks a smaller variability in TWS simulations across GCMs or
 181 GHMs/LSMs.

182

183

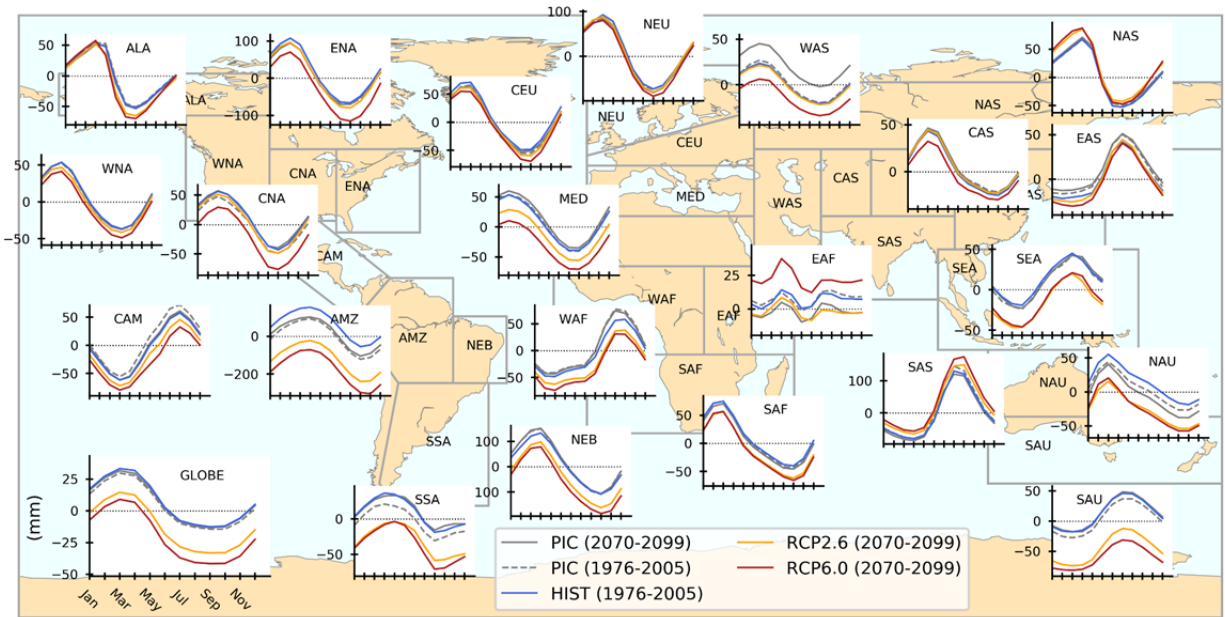
184 **Regional variability and seasonality in TWS projections**

185 The projected changes in the seasonal cycle of TWS also vary across regions (Fig. 3). Regions
186 (Supplementary Fig. 3) including the Amazon, South Europe/Mediterranean (MED), North
187 Australia (NAU), North-East Brazil, South Australia/New Zealand (SAU), Southeastern South
188 America (SSA), and West Africa (WAF) are projected to experience a decline in TWS across all
189 seasons. In regions such as Alaska, a slight increase is observed during winter months—likely
190 due to an increase in snow amount—but a discernible decline during summer-to-fall months,
191 potentially caused by a warming-driven increase in evapotranspiration. In regions where TWS is
192 expected to increase, changes in the seasonal cycle vary. While South Asia (SAS) could
193 experience an increase in TWS across all seasons, increases are projected only during late-fall to
194 early-spring in North Asia (NAS); in East Africa (EAF) increases are expected in all seasons but
195 only under RCP6.0. Many of the regions projected to experience an increase in TWS overlap
196 with regions with higher future precipitation (Extended Data Fig. 3). We find the strong drying
197 in MED to be consistent with the historically-observed north (wet)-south (dry) contrast in pan-
198 European river flows⁴⁰, implying that the regions with historical drying trends are expected to
199 become even drier under climate change. Our results for the Amazon also corroborate the widely
200 discussed drying and dry season lengthening⁴¹, suggesting that the findings are robust for this
201 region, and add to the long-standing debate on the fate of the Amazonian rainforest under a
202 warmer-drier future⁴².

203
204 Soil moisture alone has been used previously as an indicator of total TWS, on the basis that its
205 variability constitutes a large portion of the total TWS variability²⁶. We find that the component
206 contribution ratio (CCR; Methods) of soil moisture to total TWS varies substantially among
207 SREX regions. Generally, soil moisture contribution is high (>50%) in relatively dry regions,
208 including Central America/Mexico (CAM), MED, West Asia (WAS), Central Asia (CAS),
209 WAF, Southern Africa (SAF), and SAU, and low in relatively humid and snow-dominated
210 regions including Alaska, NAS, and Amazon (Extended Data Fig. 6), as also noted by previous
211 studies^{16,43}. The results suggest that soil moisture could not be used to substitute TWS globally.

212
213 The changes in TWS are driven primarily by climate forcing, as opposed to land-water
214 management and/or socio-economic drivers (see Methods). This is apparent from comparing the
215 HIST and RCP simulations with the PIC simulations (see Methods) for the baseline period and
216 late-21st century (Fig. 3). Since the PIC simulations use identical socio-economic scenarios as the
217 HIST and RCP simulations for the respective periods (Supplementary Table 2), the PIC (2070-
218 2099) versus PIC (1976-2005) comparison suggests that TWS would have remained generally
219 stable in most regions under a pre-industrial climate. Differences between the two simulations
220 can, however, be seen in some regions (e.g., EAF, SSA, WAS) even though the difference in the
221 global average is relatively small (Fig. 3). Globally, this difference is ~11% of the difference
222 between RCP6.0 (2070-2099) and PIC (1976-2005), meaning that ~90% of the projected change
223 could be attributed to climate change. A decrease in TWS is projected under pre-industrial
224 climate in CAM, EAF, and NAU. Other regions including Central North America (CAN),
225 Amazon, SSA, WAS, and SAU would have been wetter in the future under pre-industrial
226 climate. These results suggest that while the wetting caused by climate change could be offset by
227 human land-water management and socio-economic drivers in some regions (e.g., EAF), the
228 climate-induced drying could be further exacerbated by human activities in others (e.g., NAU).

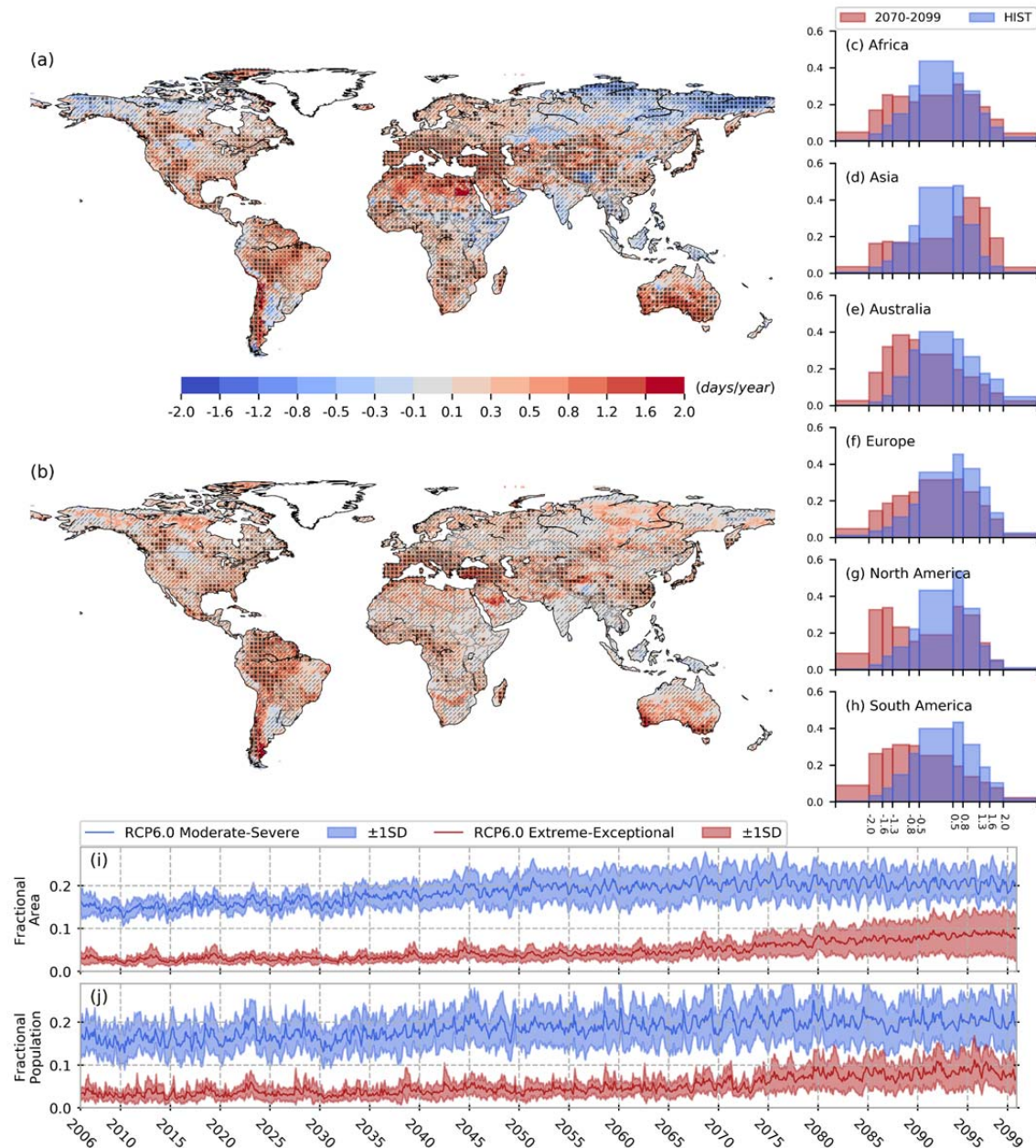
229



230
 231 **Fig. 3 | Seasonal TWS variations averaged over the selected IPCC SREX regions.** The seasonal cycle
 232 (weighted mean; same continental weights are used for all simulations) is estimated from the TWS time
 233 series for the respective periods (see legends), but the anomalies are calculated by using the mean for
 234 1861-2099 period, generated by combining the results from HIST simulations with the corresponding
 235 RCP scenario. Labels and unit are shown in the inset for the entire globe. A description of SREX regions
 236 is provided in Supplementary Fig. 3.

237
 238 **Future projection of TWS drought**

239 The projected changes in TWS correspond with shifts in future drought occurrence and severity.
 240 Many regions are projected to experience an increased occurrence of moderate-to-severe
 241 ($-0.8 \leq \text{TWS-DSI} < -1.6$) and extreme-to-exceptional ($\text{TWS-DSI} \leq -1.6$; see Methods and
 242 Supplementary Table 1) droughts (Figs. 4a and b). The direction of change is robust among
 243 ensemble members, especially in regions that are projected to experience an increase in the
 244 number of drought days (e.g., Amazon, Mediterranean, conterminous U.S., Southeast Asia, and
 245 parts of Australia). By the late-21st century (RCP6.0), the frequency of moderate, severe,
 246 extreme, and exceptional droughts is projected to increase substantially (17-34%; Supplementary
 247 Table 4) in all continents but Asia (Figs. 4c and 4e-h). This is caused largely by a significant
 248 reduction in the frequency of near-normal to abnormally dry and slightly wet conditions in
 249 Africa, and North America, primarily of wet conditions in Europe, and that of near-normal and
 250 wet conditions in South America and Australia. Further, results suggest a general reduction in the
 251 frequency of wet conditions globally except in Asia and, to some extent, in Africa. Asia stands
 252 out among all continents where the frequency of severe, extreme, and exceptional droughts as
 253 well as that of moderately wet to exceptionally wet conditions is projected to increase, caused by
 254 a reduced frequency of near-normal and slightly dry and wet conditions (Fig. 4d).
 255



256
 257
 258
 259
 260
 261
 262
 263
 264
 265
 266
 267
 268

Fig. 4 | Projected changes in occurrence and time evolution of droughts under RCP6.0. The maps show the trend (days/year) in the frequency of moderate-to-severe (a) and extreme-to-exceptional (b) droughts for the 2006–2099 period. Single and double hatches show regions where >50% and >75% of the ensemble members, respectively, agree in the sign of change. Stippling marks regions where >50% of ensemble members show a significant trend (Mann-Kendall test at 5% significance level). The histograms on the right (c–h) show the frequency of droughts with varying severity indicated by monthly TWS-DSI on the x-axis (see Methods and Supplementary Tables 1 and 4), averaged over the continents for the baseline period (HIST; 1976–2005) and late-21st century (2070–2099). The bottom panels present the change in fractional global land area (excluding Greenland, Antarctica) (i) and population projections under SSP2 (j) to experience moderate-to-severe (blue) and extreme-to-exceptional (red) droughts; shaded areas indicate ± 1 standard deviation (SD) from the ensemble mean, representing the spread in the projection among ensemble members. Results for RCP2.6 are shown in the Supplementary Fig. 4.

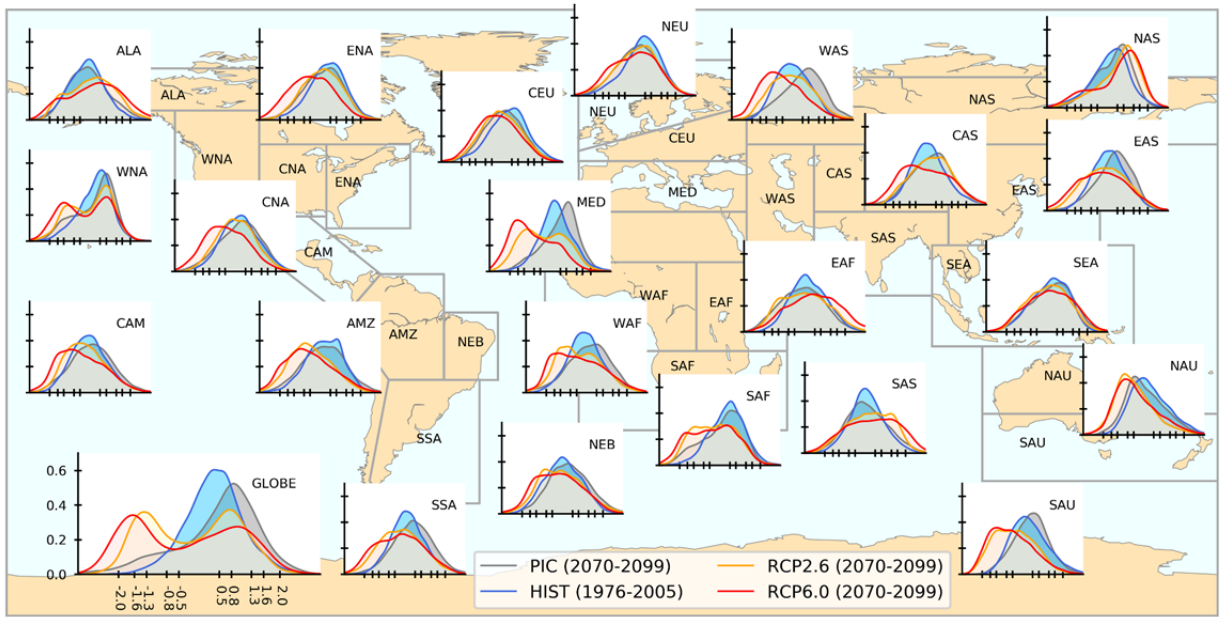
269 The global land area and projected future population (see Methods) exposed to moderate-to-
270 severe drought are projected to increase steadily until the mid-21st century and remain relatively
271 stable during the late-21st century. However, those under extreme-to-exceptional drought are
272 projected to increase until the end of the century (Figs. 4i-j) with a noticeable increase in inter-
273 ensemble spread toward the late-century, consistent with the increase in GHM/LSM uncertainty
274 (Fig. 2). Under RCP6.0, the global land area in moderate-to-severe (extreme-to-exceptional)
275 drought increases from 15% (3%) during the baseline period of 1976-2005 to 18% (4%) and
276 20% (7%), respectively, by the mid- and late-21st century. The proportion of the projected global
277 population in moderate-to-severe (extreme-to-exceptional) drought increases from 15% (3%) to
278 18% (4%) and 20% (8%) by the mid- and late-21st century, respectively, closely following the
279 changes in land area. When accounting for the projected future population, these changes are
280 equivalent to an increase in global population under moderate-to-severe (extreme-to-exceptional)
281 droughts, by ~600 (~154) and ~859 (~488) million by the mid- and late-century, respectively.
282 Further, the global population in moderate-to-severe (extreme-to-exceptional) drought for at least
283 30 days/year increases from 59% (19%) to 63% (27%), and that for at least 60 days/year
284 increases from 45% (11%) to 49% (18%) from the mid to the late-21st century.

285
286 At the regional scale, the frequency of extreme and exceptional droughts is projected to increase
287 by the late-21st century in most SREX regions (Fig. 5; Methods). The changes in drought
288 frequency are evident under both RCPs but are generally more pronounced under RCP 6.0.
289 Overall, the probability density functions (PDFs) characterized by a symmetrical distribution
290 (centered at TWS-DSI=0) for the historical period tend to become more positively skewed in
291 most regions where TWS is expected to decline (see Figs. 1 and 3), meaning that these regions
292 are likely to experience more frequent and intense droughts in the future. For example, in the
293 Amazon the occurrence of severe, extreme, and exceptional droughts (Supplementary Table 1)
294 increases substantially (under both RCPs) by the mid and late-21st century (Fig. 5). Given that
295 the dry-season TWS deficit in the Amazon has been suggested to be increasing, causing more
296 frequent and intense droughts^{20,44}, our findings highlight that the drying would further intensify,
297 which has important implications for the resilience of the Amazonian rainforest.

298
299 Distributions with obvious positive skew for the future periods can be observed in CAM, CNA,
300 MED, NAU, SAU, WAF, and WAS. Conversely, regions such as EAF, NAS, and SAS are
301 projected to experience a reduced frequency of TWS droughts. For West North America and the
302 entire globe, a shift in the PDFs to a bimodal distribution can be seen, suggesting an increased
303 frequency of both TWS droughts and anomalously wet conditions, which further indicates a
304 reduced TWS buffer capacity under future climate. Finally, results indicate that in the absence of
305 greenhouse gas forcing (i.e., PIC simulation; Fig. 5), droughts in the future would have not
306 changed noticeably from the historical period, or drought severity could have even reduced, in
307 many regions, suggesting that the exacerbations in drought conditions are attributable primarily
308 to climate change.

309
310 A comparison of TWS-DSI with traditional drought indices (Methods; Extended Data Figs. 7-
311 10) suggests that TWS-DSI provides new information on future droughts. Unlike SRI that is
312 highly correlated with SPI, TWS-DSI exhibits different PDFs in most SREX regions (Fig. 5 and
313 Extended Data Figs. 7-8) because TWS-DSI encompasses all relevant storage components
314 related to drought, and accounts for human land-water management that directly alters water

315 availability. We find that TWS-DSI also differs from soil moisture-based indices (Fig. 5 and
 316 Extended Data Figs. 9-10) because soil moisture contribution to total TWS varies significantly
 317 among global regions (Extended Data Fig. 6); TWS-DSI captures the effects of groundwater and
 318 surface water storages and accounts for human land-water management activities not reflected in
 319 the other indices. These comparisons—supported by previous studies on historical
 320 droughts^{6,36,37}—indicate that TWS-DSI could be used synergistically with traditional drought
 321 indices to better understand and predict droughts by accounting for the role of groundwater and
 322 human activities.
 323
 324



325
 326 **Fig. 5 | Probability density function of monthly TWS-DSI for IPCC SREX regions.** Shown are
 327 ensemble simulations grouped for different cases (i.e., HIST, PIC, RCP2.6, and RCP6.0). Labels are
 328 indicated in the inset for the entire globe; x-axis labels indicate TWS-DSI (Supplementary Table 1). A
 329 description of SREX regions (background map) is provided in Supplementary Fig. 3. Similar results for
 330 the mid-21st century are shown in Supplementary Fig. 5.

331
 332 **Summary and implications**

333 The results show that climate change could reduce TWS in many regions, especially the southern
 334 hemisphere, the U.S., and southwestern Europe; exceptions are regions with high increases in
 335 precipitation, including east Africa and northern Asia. By the late-21st century and under
 336 RCP6.0, two-third of the global land could experience a reduction in TWS. We find strong
 337 agreement among ensemble model projections, especially in the direction of change, suggesting
 338 that the results are robust. We further show that extreme droughts are expected to become more
 339 frequent in most of the SREX regions. Globally, land area and projected population in extreme-
 340 to-exceptional TWS drought are projected to increase from 3% to 7% and 8%, respectively, by
 341 the late-21st century, more than doubling from that during the 1976-2005 baseline period. We use
 342 state-of-the-art models and best data available globally; yet, there are limitations to our approach.
 343 First, even though the GHMs/LSMs reproduce historical TWS variability well, these models and

344 the forcing data from GCMs contain inherent biases⁹. Second, assessment of the relative
345 contributions of individual TWS components is limited to soil moisture because the other
346 components are not currently available from ISIMIP2b simulations. Lastly, the implications of
347 vegetation response to rising CO₂ levels on TWS and drought projections are not considered
348 because the hydrological models (except LPJmL) do not currently simulate vegetation dynamics.
349 Studies have shown that elevated atmospheric CO₂ levels lead to increased leaf-level water use
350 efficiency, potentially ameliorating the reduction in water availability through reduced
351 evapotranspiration and increased soil moisture and runoff (e.g., refs.^{45,46}). These findings imply
352 that the projected decline in TWS and increase in future droughts could have potentially been
353 overestimated in our study. However, numerous other studies have shown that increased foliage
354 area under elevated CO₂ levels and warmer climate generally lead to increased vegetation growth
355 and associated water use, resulting in decreased water availability by counterbalancing the
356 increase in runoff from water-use efficiency gains^{47,48}. Thus, a comprehensive analysis of TWS
357 projections using coupled hydrological-dynamic vegetation models is required for a robust
358 estimation of the implications of vegetation response to elevated CO₂ levels, which should be a
359 priority for future studies. Despite some limitations, our study provides the first comprehensive
360 assessment of climate impacts on future TWS and droughts. Given large uncertainties and
361 medium confidence in drought projections using traditional drought indices⁴⁹, this study presents
362 a new approach to studying droughts and furthers knowledge on drought projections. Since no
363 single drought index can capture the diverse set of drought impacts from climate change⁵⁰, our
364 results provide information crucial for better predicting future droughts and understanding their
365 impacts on water resources and vegetation growth^{6,36,37}.

366
367

368 **References**

- 369 1 Rodell, M. *et al.* Emerging trends in global freshwater availability. *Nature* **557**, 651 (2018).
- 370 2 Tapley, B. D. *et al.* Contributions of GRACE to understanding climate change. *Nature Climate*
371 *Change*, 1 (2019).
- 372 3 Thomas, A. C., Reager, J. T., Famiglietti, J. S. & Rodell, M. A GRACE - based water storage
373 deficit approach for hydrological drought characterization. *Geophysical Research Letters* **41**,
374 1537-1545 (2014).
- 375 4 Houborg, R., Rodell, M., Li, B., Reichle, R. & Zaitchik, B. F. Drought indicators based on
376 model - assimilated Gravity Recovery and Climate Experiment (GRACE) terrestrial water
377 storage observations. *Water Resources Research* **48** (2012).
- 378 5 Zhao, M., Velicogna, I. & Kimball, J. S. Satellite observations of regional drought severity in the
379 continental United States using GRACE-based terrestrial water storage changes. *J. Climate* **30**,
380 6297-6308 (2017).
- 381 6 Long, D. *et al.* GRACE satellite monitoring of large depletion in water storage in response to the
382 2011 drought in Texas. *Geophysical Research Letters* **40**, 3395-3401 (2013).
- 383 7 Reager, J., Thomas, B. & Famiglietti, J. River basin flood potential inferred using GRACE
384 gravity observations at several months lead time. *Nature Geoscience* **7**, 588 (2014).
- 385 8 Pokhrel, Y. *et al.* Model estimates of sea-level change due to anthropogenic impacts on terrestrial
386 water storage. *Nature Geoscience* **5**, 389-392, doi:10.1038/ngeo1476 (2012).
- 387 9 Scanlon, B. R. *et al.* Global models underestimate large decadal declining and rising water
388 storage trends relative to GRACE satellite data. *PNAS*, 201704665 (2018).

- 389 10 Reager, J. *et al.* A decade of sea level rise slowed by climate-driven hydrology. *Science* **351**, 699-
390 703 (2016).
- 391 11 Wang, J. *et al.* Recent global decline in endorheic basin water storages. *Nature geoscience* **11**,
392 926 (2018).
- 393 12 Pokhrel, Y. *et al.* Incorporation of groundwater pumping in a global Land Surface Model with the
394 representation of human impacts. *Water Resources Research* **51**, 78-96,
395 doi:10.1002/2014WR015602 (2015).
- 396 13 Wada, Y. *et al.* Human–water interface in hydrological modelling: current status and future
397 directions. *Hydrol. Earth Syst. Sci.* **21**, 4169-4193, doi:10.5194/hess-21-4169-2017 (2017).
- 398 14 Döll, P., Müller Schmied, H., Schuh, C., Portmann, F. T. & Eicker, A. Global-scale assessment of
399 groundwater depletion and related groundwater abstractions: Combining hydrological modeling
400 with information from well observations and GRACE satellites. *Water Resources Research* **50**,
401 5698-5720, doi:10.1002/2014WR015595 (2014).
- 402 15 Hanasaki, N., Yoshikawa, S., Pokhrel, Y. & Kanae, S. A global hydrological simulation to
403 specify the sources of water used by humans. *Hydrol. Earth Syst. Sci.* **22**, 789-817,
404 doi:10.5194/hess-22-789-2018 (2018).
- 405 16 Felfelani, F., Wada, Y., Longueuevigne, L. & Pokhrel, Y. Natural and human-induced terrestrial
406 water storage change: A global analysis using hydrological models and GRACE. *Journal of*
407 *Hydrology* **553**, 105-118 (2017).
- 408 17 Rodell, M., Velicogna, I. & Famiglietti, J. S. Satellite-based estimates of groundwater depletion
409 in India. *Nature* **460**, 999-1002, doi:10.1038/nature08238 (2009).
- 410 18 Scanlon, B. R. *et al.* Groundwater depletion and sustainability of irrigation in the US High Plains
411 and Central Valley. *PNAS* **109**, 9320-9325, doi:10.1073/pnas.1200311109 (2012).
- 412 19 Famiglietti, J. S. *et al.* Satellites measure recent rates of groundwater depletion in California's
413 Central Valley. *Geophysical Research Letters* **38**, L03403, doi:10.1029/2010GL046442 (2011).
- 414 20 Chaudhari, S., Pokhrel, Y., Moran, E. & Miguez-Macho, G. Multi-decadal hydrologic change and
415 variability in the Amazon River basin: understanding terrestrial water storage variations and
416 drought characteristics. *Hydrol. Earth Syst. Sci.* **23**, 2841-2862, doi:10.5194/hess-23-2841-2019
417 (2019).
- 418 21 Schewe, J. *et al.* Multimodel assessment of water scarcity under climate change. *PNAS* **111**,
419 3245-3250, doi:10.1073/pnas.1222460110 (2014).
- 420 22 Oki, T. & Kanae, S. Global Hydrological Cycles and World Water Resources. *Science* **313**, 1068-
421 1072, doi:10.1126/science.1128845 (2006).
- 422 23 Ferguson, C., Pan, M. & Oki, T. The effect of global warming on future water availability:
423 CMIP5 synthesis. *Water Resources Research* **54**, 7791-7819 (2018).
- 424 24 Pokhrel, Y., Fan, Y. & Miguez-Macho, G. Potential hydrologic changes in the Amazon by the
425 end of the 21st century and the groundwater buffer. *Environmental Research Letters* **9**,
426 doi:10.1088/1748-9326/9/8/084004 (2014).
- 427 25 Jensen, L., Eicker, A., Dobslaw, H., Stacke, T. & Humphrey, V. Long - term wetting and drying
428 trends in land water storage derived from GRACE and CMIP5 models. *J. Geophys. Res. Atmos.*
429 (2019).
- 430 26 Freedman, F. R., Pitts, K. L. & Bridger, A. F. Evaluation of CMIP climate model hydrological
431 output for the Mississippi River Basin using GRACE satellite observations. *Journal of Hydrology*
432 **519**, 3566-3577 (2014).
- 433 27 Nasrollahi, N. *et al.* How well do CMIP5 climate simulations replicate historical trends and
434 patterns of meteorological droughts? *Water Resources Research* **51**, 2847-2864 (2015).
- 435 28 Mach, K. J. *et al.* Climate as a risk factor for armed conflict. *Nature*, 1 (2019).
- 436 29 McKee, T. B., Doesken, N. J. & Kleist, J. in *Proceedings of the 8th Conference on Applied*
437 *Climatology*. 179-183 (Boston).
- 438 30 Palmer, W. (1965).

439 31 Samaniego, L., Kumar, R. & Zink, M. Implications of parameter uncertainty on soil moisture
440 drought analysis in Germany. *Journal of Hydrometeorology* **14**, 47-68 (2013).

441 32 Sheffield, J. & Wood, E. F. Projected changes in drought occurrence under future global warming
442 from multi-model, multi-scenario, IPCC AR4 simulations. *Climate Dynamics* **31**, 79-105,
443 doi:10.1007/s00382-007-0340-z (2008).

444 33 Shukla, S. & Wood, A. W. Use of a standardized runoff index for characterizing hydrologic
445 drought. *Geophysical research letters* **35** (2008).

446 34 Dai, A. Increasing drought under global warming in observations and models. *Nature climate
447 change* **3**, 52-58 (2013).

448 35 Van Loon, A. F. Hydrological drought explained. *WIREs Water* **2**, 359-392 (2015).

449 36 Du, J. *et al.* Multicomponent Satellite Assessment of Drought Severity in the Contiguous United
450 States From 2002 to 2017 Using AMSR - E and AMSR2. *Water Resources Research* **55**, 5394-
451 5412 (2019).

452 37 Geruo, A. *et al.* Satellite-observed changes in vegetation sensitivities to surface soil moisture and
453 total water storage variations since the 2011 Texas drought. *Environmental Research Letters* **12**,
454 054006 (2017).

455 38 Frieler, K. *et al.* Assessing the impacts of 1.5 °C global warming – simulation protocol of the
456 Inter-Sectoral Impact Model Intercomparison Project (ISIMIP2b). *Geosci. Model Dev.* **10**, 4321-
457 4345, doi:10.5194/gmd-10-4321-2017 (2017).

458 39 Sanderson, B. M., Wehner, M. & Knutti, R. Skill and independence weighting for multi-model
459 assessments. *Geosci. Model Dev.* **10**, 2379-2395, doi:10.5194/gmd-10-2379-2017 (2017).

460 40 Gudmundsson, L., Seneviratne, S. I. & Zhang, X. Anthropogenic climate change detected in
461 European renewable freshwater resources. *Nature Climate Change* **7**, 813 (2017).

462 41 Boisier, J. P., Ciais, P., Ducharne, A. & Guimberteau, M. Projected strengthening of Amazonian
463 dry season by constrained climate model simulations. *Nature Climate Change* **5**, 656-660 (2015).

464 42 Malhi, Y. *et al.* Climate change, deforestation, and the fate of the Amazon. *science* **319**, 169-172
465 (2008).

466 43 Getirana, A., Kumar, S., Giroto, M. & Rodell, M. Rivers and floodplains as key components of
467 global terrestrial water storage variability. *Geophysical Research Letters* **44**, 10,359-310,368
468 (2017).

469 44 Jiménez-Muñoz, J. C. *et al.* Record-breaking warming and extreme drought in the Amazon
470 rainforest during the course of El Niño 2015–2016. *Scientific reports* **6**, 33130 (2016).

471 45 Berg, A. *et al.* Land–atmosphere feedbacks amplify aridity increase over land under global
472 warming. *Nature Climate Change* **6**, 869-874 (2016).

473 46 Lemordant, L., Gentine, P., Swann, A. S., Cook, B. I. & Scheff, J. Critical impact of vegetation
474 physiology on the continental hydrologic cycle in response to increasing CO₂. *PNAS* **115**, 4093-
475 4098 (2018).

476 47 Mankin, J. S., Seager, R., Smerdon, J. E., Cook, B. I. & Williams, A. P. Mid-latitude freshwater
477 availability reduced by projected vegetation responses to climate change. *Nature Geoscience* **12**,
478 983-988 (2019).

479 48 Singh, A., Kumar, S., Akula, S., Lawrence, D. M. & Lombardozzi, D. L. Plant growth nullifies
480 the effect of increased water - use efficiency on streamflow under elevated CO₂ in the
481 Southeastern United States. *Geophysical Research Letters* **47**, e2019GL086940 (2020).

482 49 Seneviratne, S. I. *et al.* in *Managing the Risks of Extreme Events and Disasters to Advance
483 Climate Change Adaptation* (ed C. B. Field) 109-230 (Cambridge University Press, 2017).

484 50 Wanders, N., Loon, A. F. V. & Van Lanen, H. A. Frequently used drought indices reflect
485 different drought conditions on global scale. *Hydrology and Earth System Sciences Discussions*,
486 1-16 (2017).

487

488 **Methods**

489 **Models, simulation settings, and forcing data.** The seven terrestrial hydrology models used in
490 this study include five global hydrological models (GHMs⁵¹): CWatM⁵², H08^{15,53,54}, MPI-HM⁵⁵,
491 PCR-GLOBWB⁵⁶, and WaterGAP2⁵⁷; one global land surface model (LSM⁵¹): CLM4.5⁵⁸; and
492 one dynamic global vegetation model (DGVM): LPJmL⁵⁹. All models simulate the key terrestrial
493 hydrological (e.g., soil, vegetation, river) processes (Supplementary Table 3). Meteorological
494 forcing data are derived from climate simulations by four of the GCMs (a subset of models
495 participating in the Coupled Model Intercomparison Project Phase 5; CMIP5) included in the
496 Fifth Assessment Report (AR5) of the Intergovernmental Panel on Climate Change (IPCC):
497 GFDL-ESM2M, HadGEM2-ES, IPSL-CM5A-LR, and MIROC5. The climate variables included
498 in the forcing data are precipitation, air temperature, solar radiation (short and long wave), wind
499 speed, specific humidity, and surface pressure, which are bias adjusted⁶⁰ and downscaled to
500 0.5°×0.5° spatial resolution of the terrestrial hydrology models. A comprehensive description of
501 bias adjustment and downscaling can be found in the previous literature⁶⁰⁻⁶².

502
503 For each GCM, four radiative forcing cases are considered for varying periods (Supplementary
504 Table 2): the pre-industrial control (PIC; pre-industrial climate; 1861-2099), historical climate
505 (HIST; that includes the effects of human emissions including greenhouse gases and aerosols⁶³;
506 1861-2005), low greenhouse gas concentration scenario (RCP2.6; 2006-2099), and medium-high
507 greenhouse gas concentration scenario (RCP6.0; 2006-2099). Simulations are conducted under
508 the standard protocol of the Group-2 simulation scenario design of the Inter-Sectoral Impact
509 Model Intercomparison Project phase 2b (ISIMIP2b³⁸; <https://www.isimip.org/>). The two RCPs
510 are the only RCPs for which TWS results from all models were available from ISIMIP2b
511 simulations. The hydrology models are run for each GCM-radiative forcing combination by
512 considering time-varying human land-water management activities and socio-economic
513 conditions for the HIST runs but fixed at the present day (i.e., 2005) level for future projections
514 (2006-2099; RCP2.6 and RCP6.0). For the PIC simulations, climate forcing is set at the pre-
515 industrial level and human land-water management activities and socio-economic conditions
516 vary for the historical period but are fixed at 2005 level for the future periods (see Fig. 1 in
517 Frieler et al.³⁸). Thus, while the difference between PIC and other radiative forcing cases results
518 from pure climate change, the difference between historical and future PIC runs reflects the time-
519 varying effects of human activities and socio-economic drivers, not climate change. The human
520 activities and socio-economic indicators considered are population, national gross domestic
521 product, land use and land cover change (LULCC), irrigated areas, fertilizer use, and reservoir
522 operation including water withdrawal, depending on the model schemes. LULCC and irrigated
523 areas are prescribed based on the HYDE3-MIRCA data⁶⁴⁻⁶⁶ and data for dams and reservoirs are
524 taken from the GRanD database⁶⁷. Irrigation (and other water use sector) schemes vary among
525 models (Supplementary Table 3) but all models simulate global irrigation requirements within
526 plausible limits of reported datasets based on country statistics (see reference to each model for
527 more details). The reservoir operation schemes are based on Hanasaki et al.⁶⁸ (H08 and
528 WaterGAP2), Biemans et al.⁶⁹ (LPJmL), and a combination of Haddeland et al.⁷⁰ and Adams et
529 al.⁷¹ (CWatM and PCR-GLOBWB); reservoirs are not represented in MPI-HM and CLM4.5.
530 Soil column depth and layer configuration and groundwater representation vary among models
531 (Supplementary Table 3).

532

533 **Multi-model weighted mean.** Multi-model mean is calculated by weighting the ensemble
 534 members based on their skill (i.e., the root mean squared error (RMSE) of the area-weighted
 535 seasonal cycle of TWS relative to GRACE data) and independence (i.e., a measure of how
 536 different model results are) scores, following previous studies^{39,72}. The continent-based,
 537 temporally static weights ($w_o(i)$) for the 27 ensemble members (Extended Data Fig. 1) are
 538 calculated as the normalized product of the skill and independence weights so that their sum is
 539 unity^{39,72}, i.e., $(\sum_{i=1}^{27} w_o(i) = 1)$. The independence weight of member i , $w_u(i)$, is computed as
 540 the inverse of the summation of pairwise similarity score, $S(\delta_{i,j})$, which ranges between 1 (for
 541 identical members) and 0 (for the most distinct members). Mathematically,

542
$$w_u(i) = \frac{1}{1 + \sum_{j \neq i}^{27} S(\delta_{i,j})}$$
. The pairwise similarity score is calculated as a function of the

543 Euclidean distance³⁹ between the members ($\delta_{i,j}$), represented by the RMSE of the continent-
 544 level average TWS seasonal cycle from two members, and a parameter called the radius of

545 similarity (D_u):
$$S(\delta_{i,j}) = \exp\left(-\left(\frac{\delta_{i,j}}{D_u}\right)^2\right)$$
, where $\delta_{i,j}$ is normalized by the mean of pairwise inter-

546 model distances (Extended Data Fig. 2). The parameter D_u is the distance below which models
 547 are marked as similar and is resolved for each continent as a fraction of the distance between the
 548 best performing member (i.e., the model with the smallest RMSE) and GRACE through an
 549 iterative process³⁹. The skill weighting of member i , $w_q(i)$, is calculated based on the stretched
 550 exponential function⁷³ of the distance from GRACE ($\delta_{i,GRACE}$; the normalized RMSE of
 551 member i 's TWS seasonal cycle against GRACE for 2002-2016) and the radius of model quality

552
$$(D_q): w_q(i) = \exp\left(-\left(\frac{\delta_{i,GRACE}}{D_q}\right)^2\right)$$
, where smaller distances from the GRACE seasonal cycle

553 result in larger skill score/weight. The parameter D_q is also defined as a fraction of the distance
 554 between the best performing member and GRACE. This parameter controls the strength of the
 555 skill weighting. That is, when D_q approaches zero, most of the simulations get significantly
 556 down-weighted and only the best performing model is assigned a high skill score. Conversely, as
 557 D_q approaches infinity, all ensemble members are allotted a high (i.e., close to 1) skill score
 558 alike and therefore, the multi-model weighted mean approaches the non-skilled weighted mean.

559 Finally, the continent-based D_q values are estimated for 2002-2016 period and tested for
 560 RCP6.0 late-century simulations following a perfect model test and through an iterative
 561 procedure³⁹. The perfect model test is conducted to ensure that out of sample simulations (i.e.,
 562 simulations out of the GRACE period) are also improved with the weighting scheme. Note that
 563 the model weights are estimated by using the seasonal cycle of TWS, rather than the trend or
 564 inter-annual variability, because the original study³⁹ that described the weighing scheme used the
 565 seasonality of climate variables, and no studies have demonstrated the applicability or robustness

566 of the schemes based on trend or inter-annual variability. Further, the GRACE data period is
567 relatively short to rely on temporal trends, which are highly sensitive to the time window chosen.
568

569 **Simulated TWS, GRACE data, model evaluation, and TWS variability under climate**
570 **change.** The monthly-scale simulated TWS is derived by vertically integrating the surface and
571 subsurface water storages, which include snow, canopy, river, reservoir (if simulated), lake (if
572 simulated), wetland (if simulated), soil, and groundwater storages^{74,75}. TWS derived from
573 GRACE satellite measurements is used to evaluate the simulated TWS for the 2002-2016 period.
574 We use the mean of mascon products⁷⁶ from two processing centers: Center for Space Research
575 (CSR) at the University of Texas at Austin, and Jet Propulsion Laboratory (JPL) at the California
576 Institute of Technology. For model results, since the evaluation period is not covered completely
577 by HIST simulations, we combine the results from HIST simulations (2002-2005) with results
578 from RCP 2.6 (2006-2016). The seasonal mean of TWS anomalies (Extended Data Fig. 5 and
579 Supplementary Fig. 1) is derived by first calculating the climatological mean seasonal cycle of
580 TWS for the evaluation period and then taking the mean for each season. For consistency, the
581 same reference period (2002-2016) is used in calculating the seasonal anomalies for both
582 GRACE data and model simulations. Changes in TWS for the mid (2030-2059) and late (2070-
583 2099) 21st century (for the two RCPs) are calculated by taking the difference of mean TWS for
584 those periods to the mean TWS for the historical baseline period of 1976-2005, which is the last
585 30-year period of the historical simulations; simulations from year 2006 are conducted under
586 future climate scenarios.

587
588 **Quantification of uncertainty in TWS simulations.** The contribution of uncertainties from
589 GCMs (i.e., forcing data) and GHMs/LSMs to TWS is quantified by using the sequential
590 sampling approach⁷⁷. In this approach, the uncertainty contribution of GCMs and GHMs/LSMs
591 is calculated using the range statistic⁷⁷ of monthly TWS (represented as the quantile-based TWS
592 index) averaged over the SREX regions for the historical baseline period, and mid- and late-21st
593 century. The GCMs (GHMs/LSMs) uncertainty—characterized as the range of mean in the
594 quantile-based TWS index—for a given RCP scenario is computed by first averaging the
595 quantile-based TWS index across all GHMs/LSMs (GCM) for each of the GCMs (GHMs/LSMs)
596 and then calculating the range across GCMs (GHMs/LSMs). The quantile-based TWS index,
597 spatially averaged over SREX regions, is calculated³¹ by (1) fitting a non-parametric kernel
598 density function to TWS data, (2) estimating the PDF, and (3) numerically integrating the PDF
599 between zero and the simulated TWS.

600
601 **Component contribution of soil moisture to total TWS.** A dimensionless metric, the
602 component contribution ratio (CCR^{16,78}), is used to quantify the contribution of soil moisture to
603 total TWS (Extended Data Fig. 6). CCR represents the ratio of seasonal amplitude of soil
604 moisture to that of TWS. The CCR is used to assess the differences between the drought
605 projected by TWS-DSI and soil moisture drought index (SMI). The contribution of other TWS
606 components could not be examined as those variables are not currently available from ISIMIP2b
607 simulations.

608
609 **TWS Drought Severity Index (TWS-DSI) and drought severity under climate change.**
610 Monthly TWS drought severity index (TWS-DSI) is estimated for all ensemble members

611 following Zhao et al.⁵; $TWS-DSI_{i,j} = (TWS_{i,j} - \mu_j) / \sigma_j$, where $TWS_{i,j}$ is the TWS anomaly in
612 year i and month j , and μ_j and σ_j are the climatological mean and standard deviation,
613 respectively, of monthly TWS anomalies for the reference period. $TWS-DSI_{i,j}$ is a non-
614 dimensional index that defines droughts with varying degrees of severity, also representing wet
615 conditions (Supplementary Table 1). In calculating the mean and standard deviation of TWS for
616 any specified period, a common reference period set to 1861-2099 is used to avoid potential
617 exaggeration in the estimates of TWS variability and drought evolution⁷⁹, and for consistent
618 comparison. The drought trend (Figs. 4a-b) is calculated as the linear least-square trend using the
619 time series of annual drought occurrence presented in days per year. The significance of trend
620 values is evaluated using the non-parametric Mann-Kendall trend test^{80,81} with 5% significance
621 level. Note that for the trend calculations, four droughts types are re-grouped into two major
622 categories for simplicity: moderate-to-severe ($-1.6 < TWS-DSI \leq -0.8$) and extreme-to-
623 exceptional ($TWS-DSI \leq -1.6$) droughts (see Supplementary Table 1 for more details).

624
625 The frequency of droughts with varying severities used for continental-scale drought analysis
626 (Figs. 4c-h) is estimated by considering the TWS-DSI calculated for all ensemble members,
627 normalized such that the results show the probability density function (PDF) at bins
628 corresponding to the classes of drought and wet conditions (Supplementary Table 1). For the
629 analysis of global population affected by drought, we use the time-varying (2006-2100) gridded
630 global population data generated by scaling the 2005 population data from the Center for
631 International Earth Science Information Network (CIESIN) at Columbia University
632 (<https://sedac.ciesin.columbia.edu/>) with the country-level future population growth rate
633 (<https://tntcat.iiasa.ac.at/SspDb>) for the Shared Socioeconomic Pathways 2 (SSP2)⁸². Among the
634 five SSPs, SSP2 reflects an intermediate, middle of the road scenario in which population growth
635 is medium⁸³. The changes in future population under drought are estimated relative to the
636 baseline period of 1976-2005 but using static population data for 2005. Finally, the PDFs for
637 each IPCC SREX regions (Fig. 5) are estimated using the non-parametric kernel-density
638 method⁸⁴ and by considering all ensemble members. There is a bimodality in the PDF of TWS-
639 DSI in some regions as a result of preferential states in water stores such as soil moisture^{85,86},
640 thus using the non-parametric kernel-density method is more apt compared to the parametric
641 unimodal distributions with underlying assumptions such as normality^{27,31}. We find that using
642 kernel-density method to estimate the PDF of TWS-DSI results in almost identical PDF
643 estimation (not shown) to that from the conventional standardized drought indices²⁹—i.e., by
644 first fitting the TWS data to a secondary distribution (e.g., gamma, Pearson Type III) and then
645 transforming it to standard normal distribution.

646
647 The standardized precipitation index (SPI²⁹) and standardized runoff index (SRI³³) are calculated
648 by first fitting the monthly precipitation and runoff data, respectively, to the gamma distribution
649 function to obtain monthly climatological distributions for the reference period (1861-2099).
650 These distributions are then used to estimate the cumulative probability of the variable
651 (precipitation or runoff) for a certain period. Finally, the cumulative probabilities are converted
652 to standard normal deviate ($\mu = 0$ and $\sigma = 1$) by inverting the respective cumulative distribution
653 function (CDF). The SMI is estimated based on two approaches. For the direct comparison with
654 TWS-DSI, SMI is obtained using the same methodology as TWS-DSI⁵, however using soil

655 moisture data instead of TWS (Extended Data Fig. 9). Additionally, a more conventional
656 quantile-based SMI (Extended Data Fig. 10) is calculated following Samaniego et al.³¹ and
657 Sheffield and Wood³². To do so, soil moisture is first fitted to a non-parametric kernel density
658 function to derive the monthly climatological PDFs for the reference period (1861-2099). The
659 quantile-based drought index corresponding to a given soil moisture for month i (x_i) is then
660 derived by numerically integrating the respective PDF³¹ (\hat{f}) as: $SMI_i = \int_0^{x_i} \hat{f}(u)du$. The PDFs
661 of drought indices (SPI, SRI, and SMI) are generated for different periods using kernel-density
662 method (Extended Data Figs. 7-10).
663

664 **Data Availability**

665 The model results are freely available from the ISIMIP project portal
666 (<https://www.isimip.org/outputdata/doi-isimip-data-sets/#output-data>) and the two GRACE
667 products used for model evaluation can be obtained from <http://www2.csr.utexas.edu/grace/> and
668 <https://podaac.jpl.nasa.gov/GRACE>. The final data used to generate the figures in the main text
669 are available on CUAHSI HydroShare.
670

671 **Code Availability**

672 All figures are produced using the freely available visualization library (Matplotlib) in Python
673 3.5 and statistical analysis is performed using NumPy and other built-in functions in Python 3.5.
674

675 **References**

- 676
677 51 Haddeland, I. *et al.* Multimodel Estimate of the Global Terrestrial Water Balance: Setup and First
678 Results. *Journal of Hydrometeorology* **12**, 869-884, doi:10.1175/2011JHM1324.1 (2011).
679 52 Burek, P. *et al.* Development of the Community Water Model (CWatM v1.04) A high-resolution
680 hydrological model for global and regional assessment of integrated water resources
681 management. *Geosci. Model Dev. Discuss.* **2019**, 1-49, doi:10.5194/gmd-2019-214 (2019).
682 53 Hanasaki, N. *et al.* An integrated model for the assessment of global water resources – Part 1:
683 Model description and input meteorological forcing. *Hydrol. Earth Syst. Sci.* **12**, 1007-1025,
684 doi:10.5194/hess-12-1007-2008 (2008).
685 54 Hanasaki, N. *et al.* An integrated model for the assessment of global water resources – Part 2:
686 Applications and assessments. *Hydrol. Earth Syst. Sci.* **12**, 1027-1037, doi:10.5194/hess-12-1027-
687 2008 (2008).
688 55 Stacke, T. & Hagemann, S. Development and evaluation of a global dynamical wetlands extent
689 scheme. *Hydrol. Earth Syst. Sci.* **16**, 2915-2933, doi:10.5194/hess-16-2915-2012 (2012).
690 56 Wada, Y., Wisser, D. & Bierkens, M. F. P. Global modeling of withdrawal, allocation and
691 consumptive use of surface water and groundwater resources. *Earth Syst. Dynam.* **5**, 15-40,
692 doi:10.5194/esd-5-15-2014 (2014).
693 57 Mueller Schmied, H. *et al.* Variations of global and continental water balance components as
694 impacted by climate forcing uncertainty and human water use. *Hydrology and Earth System*
695 *Sciences* **20**, 2877-2898 (2016).
696 58 Oleson, K. W. Technical Description of version 4.5 of the Community Land Model (CLM). 422
697 (National Center for Atmospheric Research, Boulder, CO, 2013).
698 59 Bondeau, A. *et al.* Modelling the role of agriculture for the 20th century global terrestrial carbon
699 balance. *Global Change Biology* **13**, 679-706, doi:10.1111/j.1365-2486.2006.01305.x (2007).

700 60 Lange, S. Trend-preserving bias adjustment and statistical downscaling with ISIMIP3BASD (v1.
701 0). *Geoscientific Model Development* **12**, 3055-3070 (2019).

702 61 Hempel, S., Frieler, K., Warszawski, L., Schewe, J. & Piontek, F. A trend-preserving bias
703 correction—the ISI-MIP approach. *Earth System Dynamics* **4**, 219-236 (2013).

704 62 Lange, S. Bias correction of surface downwelling longwave and shortwave radiation for the
705 EWEMBI dataset. *Earth System Dynamics* **9**, 627-645 (2018).

706 63 Taylor, K. E., Stouffer, R. J. & Meehl, G. A. An Overview of CMIP5 and the Experiment Design.
707 *Bull. Amer. Meteor. Soc.* **93**, 485-498, doi:10.1175/BAMS-D-11-00094.1 (2012).

708 64 Klein Goldewijk, K., Beusen, A., van Drecht, G. & de Vos, M. The HYDE 3.1 spatially explicit
709 database of human-induced global land-use change over the past 12,000 years. *Global Ecology*
710 *and Biogeography* **20**, 73-86, doi:10.1111/j.1466-8238.2010.00587.x (2011).

711 65 Portmann, F. T., Siebert, S. & Döll, P. MIRCA2000—Global monthly irrigated and rainfed crop
712 areas around the year 2000: A new high-resolution data set for agricultural and hydrological
713 modeling. *Global Biogeochem. Cycles* **24**, GB1011, doi:10.1029/2008GB003435 (2010).

714 66 Ramankutty, N., Evan, A. T., Monfreda, C. & Foley, J. A. Farming the planet: 1. Geographic
715 distribution of global agricultural lands in the year 2000. *Global Biogeochem. Cycles* **22**,
716 GB1003, doi:10.1029/2007GB002952 (2008).

717 67 Lehner, B. *et al.* High-resolution mapping of the world's reservoirs and dams for sustainable
718 river-flow management. *Frontiers in Ecology and the Environment* **9**, 494-502,
719 doi:10.1890/100125 (2011).

720 68 Hanasaki, N., Kanae, S. & Oki, T. A reservoir operation scheme for global river routing models.
721 *Journal of Hydrology* **327**, 22-41, doi:10.1016/j.jhydrol.2005.11.011 (2006).

722 69 Biemans, H. *et al.* Impact of reservoirs on river discharge and irrigation water supply during the
723 20th century. *Water Resources Research* **47**, W03509, doi:10.1029/2009WR008929 (2011).

724 70 Haddeland, I., Skaugen, T. & Lettenmaier, D. P. Anthropogenic impacts on continental surface
725 water fluxes. *Geophysical Research Letters* **33**, L08406, doi:10.1029/2006GL026047 (2006).

726 71 Adam, J. C., Haddeland, I., Su, F. & Lettenmaier, D. P. Simulation of reservoir influences on
727 annual and seasonal streamflow changes for the Lena, Yenisei, and Ob' rivers. *J. Geophys. Res.*
728 *Atmos.* **112**, D24114, doi:10.1029/2007JD008525 (2007).

729 72 Eyring, V. *et al.* Taking climate model evaluation to the next level. *Nature Climate Change*, 1
730 (2019).

731 73 Wuttke, J. Laplace–Fourier transform of the stretched exponential function: Analytic error
732 bounds, double exponential transform, and open-source implementation “libkww”. *Algorithms* **5**,
733 604-628 (2012).

734 74 Pokhrel, Y., Fan, Y., Miguez-Macho, G., Yeh, P. J. F. & Han, S.-C. The role of groundwater in
735 the Amazon water cycle: 3. Influence on terrestrial water storage computations and comparison
736 with GRACE. *J. Geophys. Res. Atmos.* **118**, 3233-3244, doi:10.1002/jgrd.50335 (2013).

737 75 Hirschi, M., Seneviratne, S. I. & Schär, C. Seasonal variations in terrestrial water storage for
738 major midlatitude river basins. *Journal of Hydrometeorology* **7**, 39-60 (2006).

739 76 Scanlon, B. R. *et al.* Global evaluation of new GRACE mascon products for hydrologic
740 applications. *Water Resources Research* **52**, 9412-9429 (2016).

741 77 Samaniego, L. *et al.* Propagation of forcing and model uncertainties on to hydrological drought
742 characteristics in a multi-model century-long experiment in large river basins. *Climatic Change*
743 **141**, 435-449 (2017).

744 78 Kim, H., Yeh, P. J. F., Oki, T. & Kanae, S. Role of rivers in the seasonal variations of terrestrial
745 water storage over global basins. *Geophysical Research Letters* **36**, L17402,
746 doi:10.1029/2009GL039006 (2009).

747 79 Sippel, S. *et al.* Quantifying changes in climate variability and extremes: Pitfalls and their
748 overcoming. *Geophysical Research Letters* **42**, 9990-9998 (2015).

749 80 Mann, H. B. Nonparametric tests against trend. *Econometrica: Journal of the Econometric*
750 *Society*, 245-259 (1945).

751 81 Kendall, M. Rank correlation measures. *Charles Griffin, London* **202**, 15 (1975).
752 82 Riahi, K. *et al.* The shared socioeconomic pathways and their energy, land use, and greenhouse
753 gas emissions implications: an overview. *Global Environmental Change* **42**, 153-168 (2017).
754 83 Knorr, W., Arneth, A. & Jiang, L. Demographic controls of future global fire risk. *Nature*
755 *Climate Change* **6**, 781 (2016).
756 84 Gatrell, A. C., Bailey, T. C., Diggle, P. J. & Rowlingson, B. S. Spatial point pattern analysis and
757 its application in geographical epidemiology. *Transactions of the Institute of British geographers*,
758 256-274 (1996).
759 85 D'Odorico, P. & Porporato, A. Preferential states in soil moisture and climate dynamics. *PNAS*
760 **101**, 8848-8851 (2004).
761 86 Laio, F., Porporato, A., Ridolfi, L. & Rodriguez - Iturbe, I. On the seasonal dynamics of mean
762 soil moisture. *J. Geophys. Res. Atmos.* **107**, ACL 8-1-ACL 8-9 (2002).
763
764
765

766 **Acknowledgements**

767 Y.P. and F.F. acknowledge the support from the National Science Foundation (CAREER Award,
768 grant #: 1752729). H.M.S. and C.E.T. acknowledge the support from the German Federal
769 Ministry of Education and Research (BMBF, grant #: 01LS1711F). J.L. acknowledges the
770 support from the Strategic Priority Research Program of Chinese Academy of Sciences (Grant
771 No. XDA20060402), the National Natural Science Foundation of China (41625001,
772 51711520317). N.H. acknowledges the support from ERTDF (2RF-1802) of the ERCA, Japan.
773 Y.W. is supported by the European Union under Horizon 2020 EUCP project (grant #: 776613)
774 and JPI Climate and European Union under ISIpedia project (grant #: 690462). W.T.
775 acknowledges the support from the Uniscientia Foundation and the ETH Zurich Foundation (Fel-
776 45 15-1).
777

778 **Author contributions**

779 Y.P. conceived the research. F.F. processed model results, conducted the analyses, and prepared
780 graphics. Y.P. and F.F. interpreted the results, and all authors discussed and commented on the
781 outcome. Y.P. prepared the draft with contribution from F.F., and all authors commented on and
782 edited the manuscript. Respective modeling groups conducted hydrological simulations under
783 the ISIMIP2b project coordinated by S.N.G. and H.M.S.
784

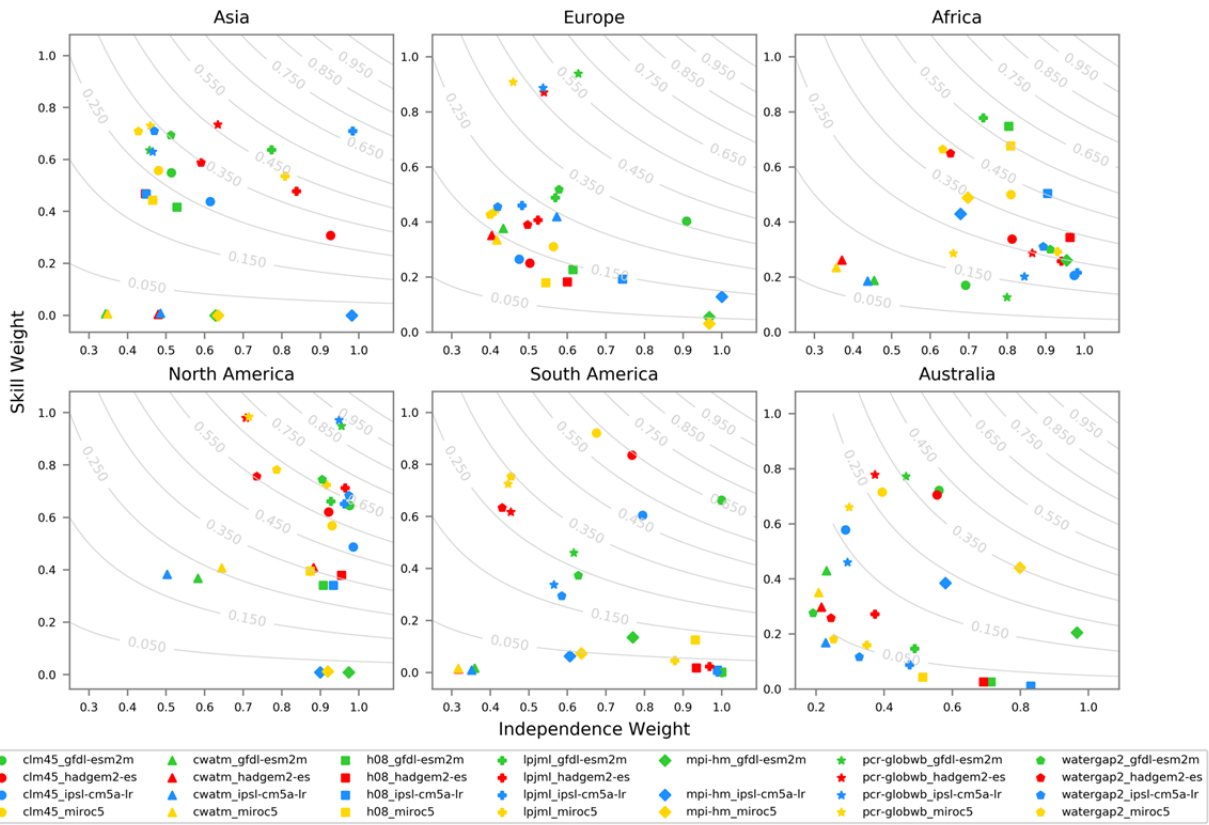
785 **Competing interests**

786 The authors declare no competing interests.
787

788 **Additional Information**

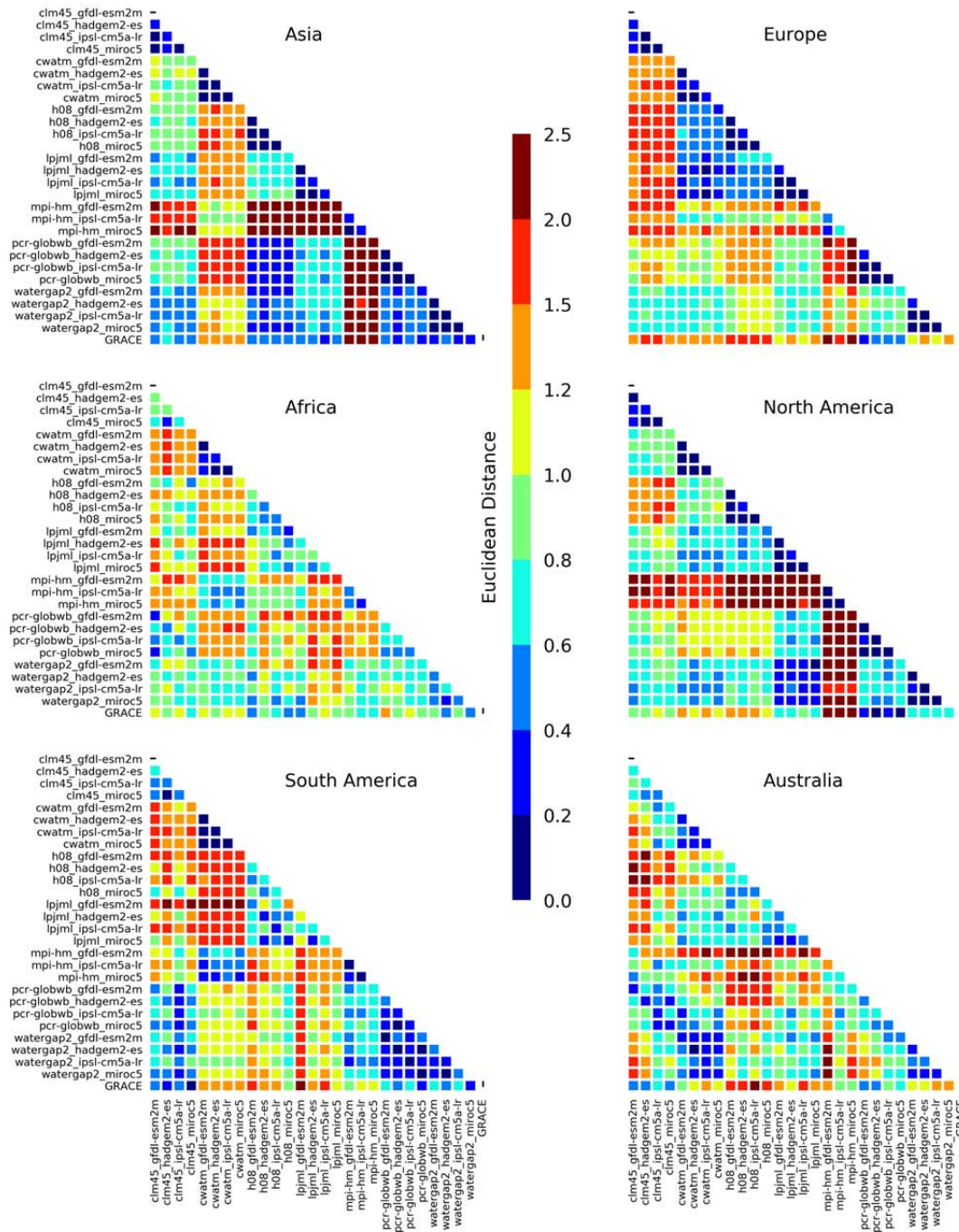
789 **Correspondence and requests for materials** should be addressed to Y.P.
790

791 **Extended Data**
 792

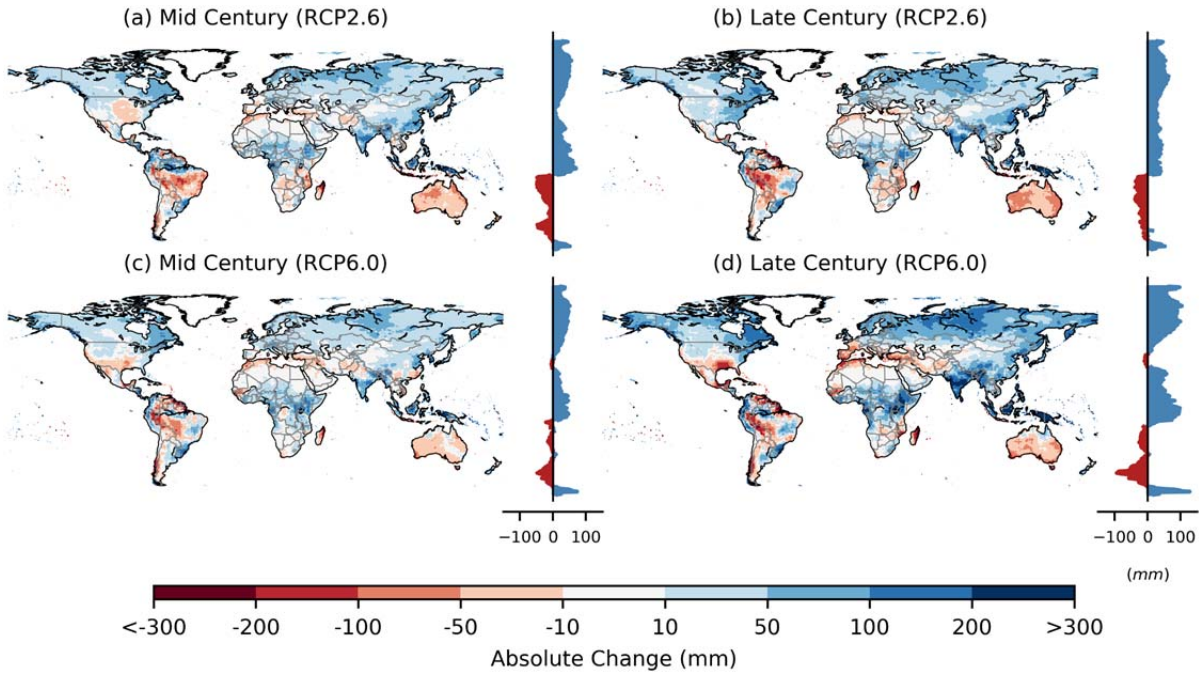


793 **Extended Data Fig. 1 | Continent-based model skill and independence weights (see Methods**
 794 **for details) for 27 ensemble members. The weights are temporally static.**
 795

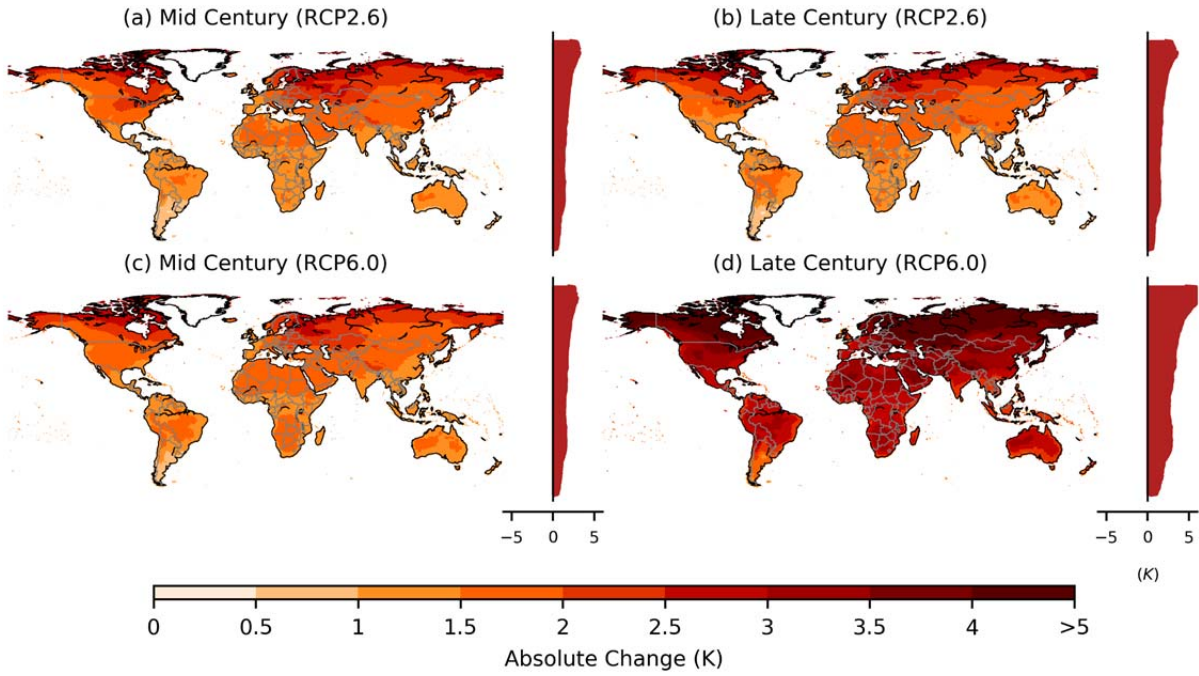
796



797
 798 **Extended Data Fig. 2 | Continent-based pairwise inter-model distance matrix for ensemble**
 799 **simulations and GRACE observations.** Each row or column associates with a single ensemble
 800 member or GRACE observations, and each cell represents a pairwise distance of that member
 801 compared to others. Distances are evaluated based on the root mean squared error (RMSE) of
 802 TWS seasonal cycle (calculated for 2002-2016 period by combining the results from HIST
 803 simulations with RCP2.6) spatially averaged over each domain (i.e., the continents). The
 804 distance for each member is normalized by the mean of pair-wise distances for all members.
 805 Lower values of the pairwise distance between two members indicate a better agreement
 806 between the two members, and vice versa.

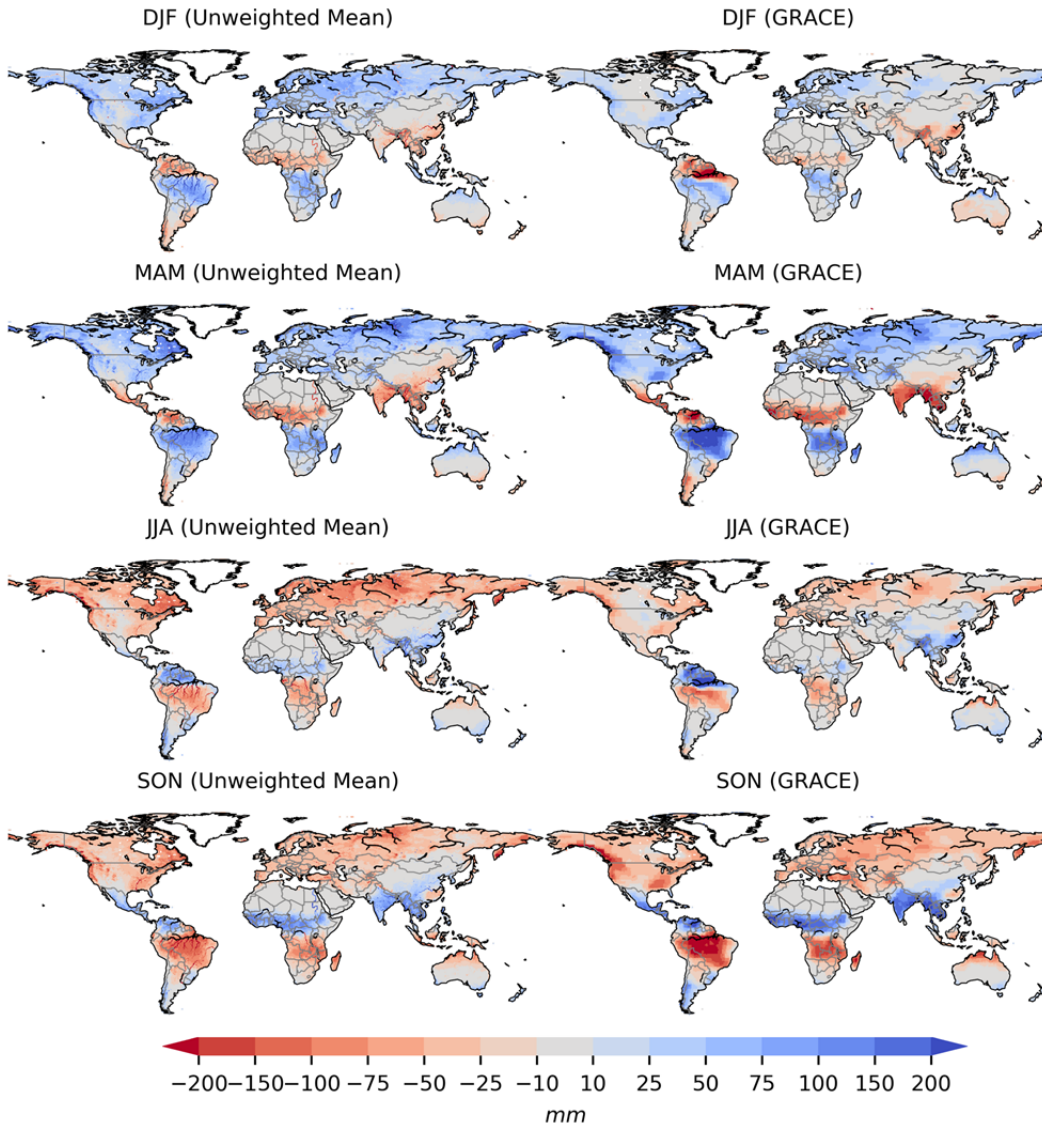


807
 808 **Extended Data Fig. 3 | Spatial patterns of change in precipitation by the mid (2030-2059)**
 809 **and late (2070-2099) 21st century under RCP 2.6 and 6.0.** Shown are the absolute differences
 810 in the 30-year mean (mm/year) between the two future periods and historical baseline period of
 811 1976-2005, calculated as the mean of the results from four Global Climate Models (GCMs) used
 812 to drive the hydrological models: HadGEM2-ES, GFDL-ESM2M, IPSL-CM5A-LR, and
 813 MIROC5. Note that Greenland is masked out. The graph on the right of each panel shows the
 814 latitudinal mean.
 815

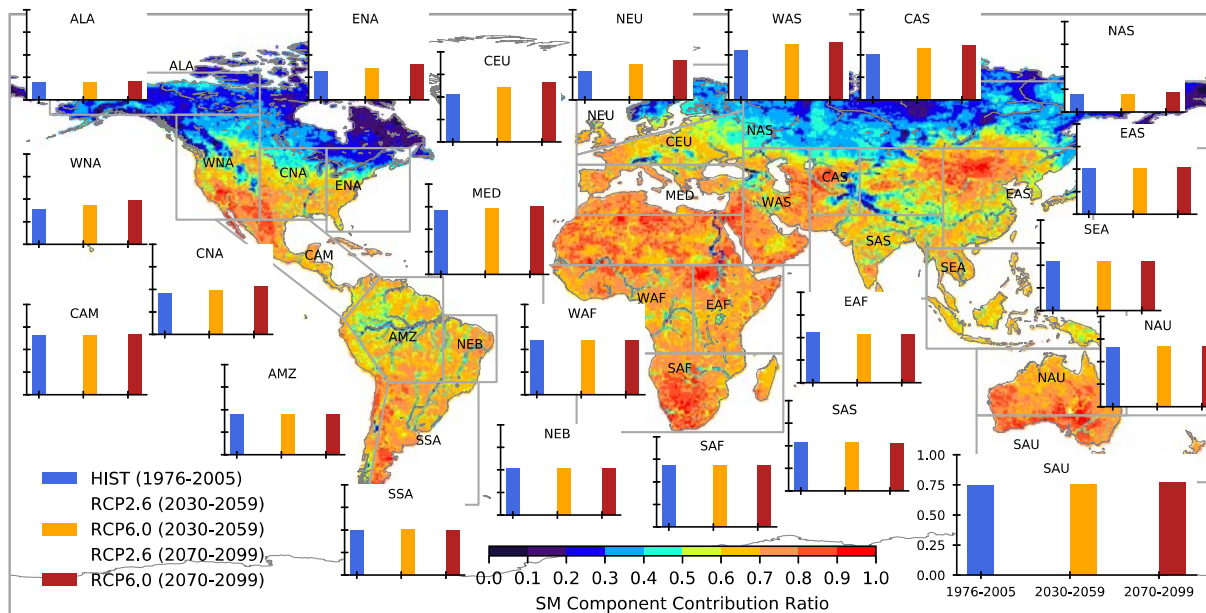


816
817
818

Extended Data Fig. 4 | Same as in Extended Data Figure 3 but for temperature (in Kelvin).

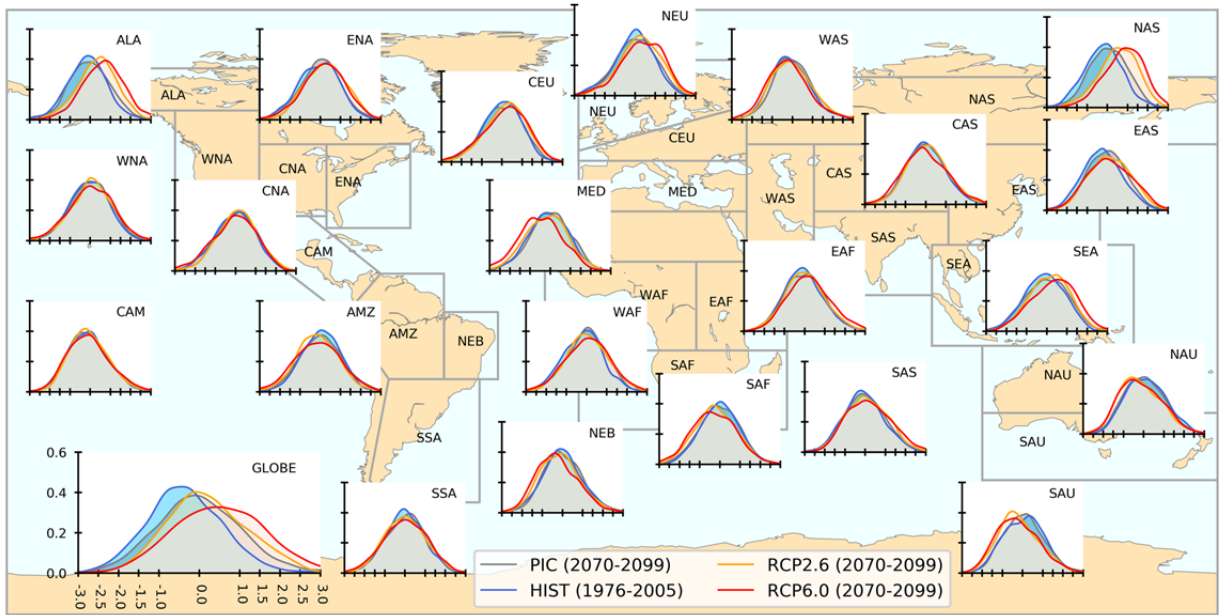


819
 820 **Extended Data Fig. 5 | Spatial patterns of seasonal TWS anomalies from models and**
 821 **GRACE data.** Shown are the seasonal averages (December-February (DJF), March-May
 822 (MAM), June-August (JJA), and September-November (SON)) of the simulated (multi-model
 823 ensemble mean) and GRACE-based monthly TWS deviation from the mean for the GRACE
 824 period (2002-2016). Model results for the 2002-2005 period are taken from the historical
 825 simulations (see Supplementary Table 2), and for 2006-2016 from RCP2.6 runs (2005soc).
 826 Anomalies are calculated by using the mean for 2002-2016 period for both model results and
 827 GRACE data. Note that we use the simple ensemble average, not the weighted mean, for these
 828 comparisons to provide an unbiased evaluation of the models and to ensure that the model-
 829 GRACE agreement is not a result of the weighting that is based on the GRACE data. The results
 830 from RCP6.0 (not shown) are almost identical to that shown here. GRACE data shown are the
 831 mean of mascon products⁷⁶ from two processing centers: the Center for Space Research (CSR) at
 832 the University of Texas at Austin (<http://www2.csr.utexas.edu/grace/>) and NASA Jet Propulsion
 833 Laboratory (JPL; <https://podaac.jpl.nasa.gov/GRACE>).



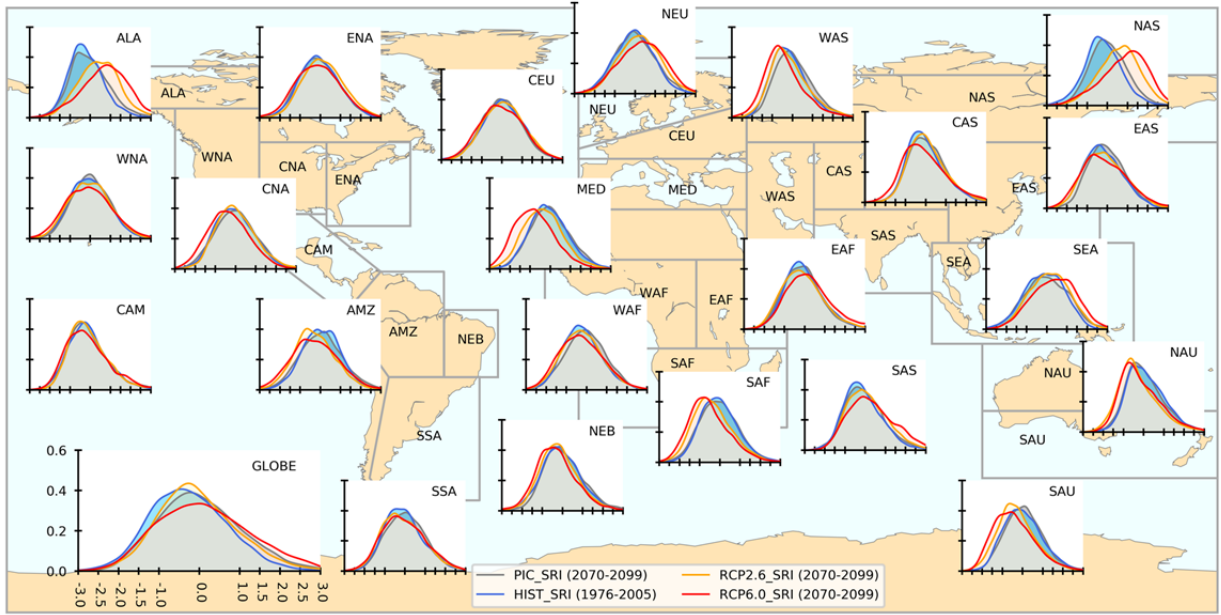
834
 835 **Extended Data Fig. 6 | Soil moisture (SM) component contribution ratio (CCR^{16,78}).** The
 836 background map depicts the spatial variability of SM CCR (the ratio of seasonal amplitude of
 837 SM to that of TWS; see Methods) based on the ensemble mean results for the historical baseline
 838 period (HIST; 1976-2005). The insets present the SM CCR averaged over the IPCC SRES
 839 regions for the historical baseline period, mid-21st century (2030-2059), and late-21st century
 840 (2070-2099); results from both RCPs (RCP 2.6 and 6.0) are shown. Evidently, and as discussed
 841 in the main text, SM CCR shows a large spatial variability.

842



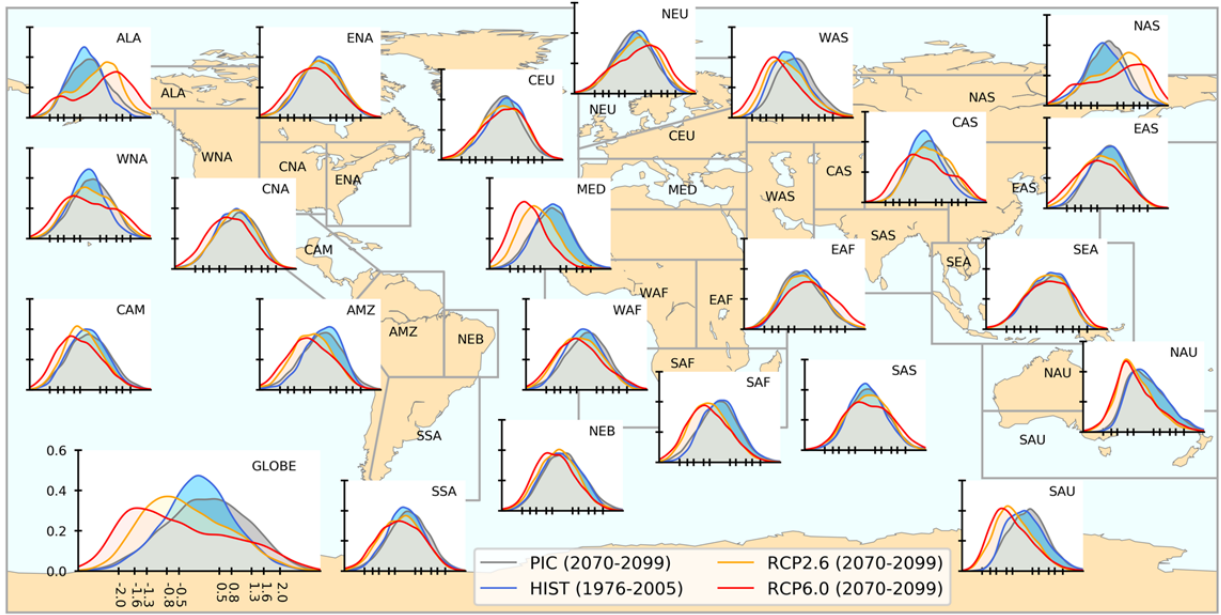
843
 844 **Extended Data Fig. 7 | Same as in Figure 5 in the main text but for standardized**
 845 **precipitation index (SPI²⁹; see Methods).**

846
 847



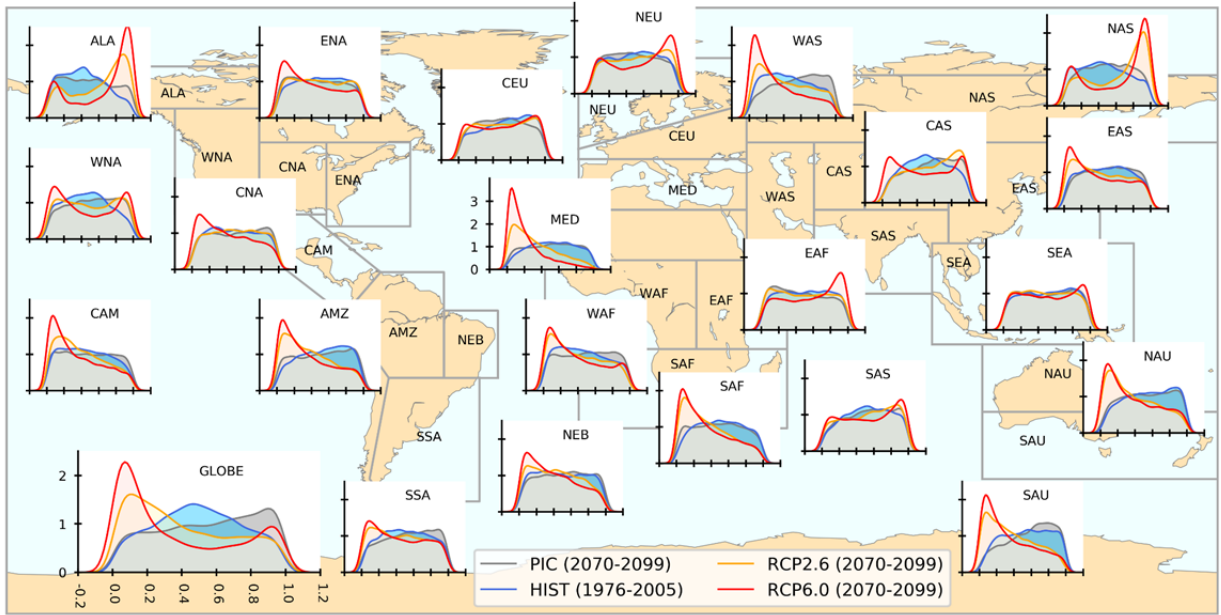
848
 849
 850
 851

Extended Data Fig. 8 | Same as in Figure 5 in the main text but for standardized runoff drought index (SRI³³; see Methods).



852
 853
 854
 855

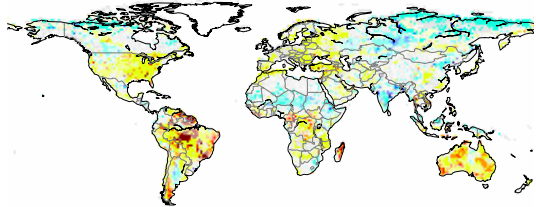
Extended Data Fig. 9 | Same as in Figure 5 in the main text but for SM drought index calculated based on Zhao et al. (ref⁵), i.e., by using only SM instead of total TWS.



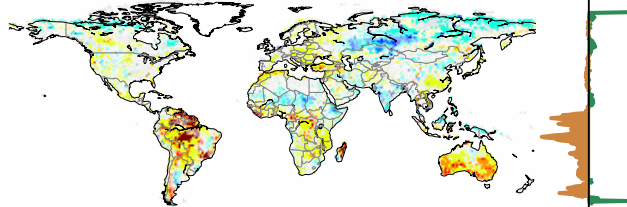
856
 857 **Extended Data Fig. 10 | Same as in Figure 5 in the main text but for SM drought index**
 858 **(SMI^{31,32}; see Methods). Note the different y-axis scale for MED.**

859

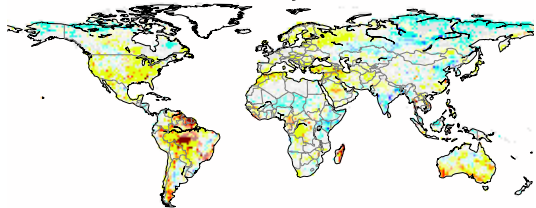
(a) Mid Century (RCP2.6)



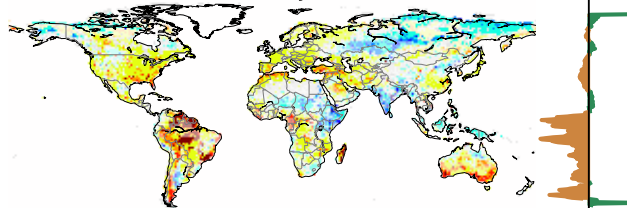
(b) Late Century (RCP2.6)



(c) Mid Century (RCP6.0)



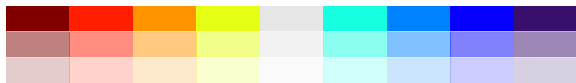
(d) Late Century (RCP6.0)



-200 0 200

-200 0 200

agreement

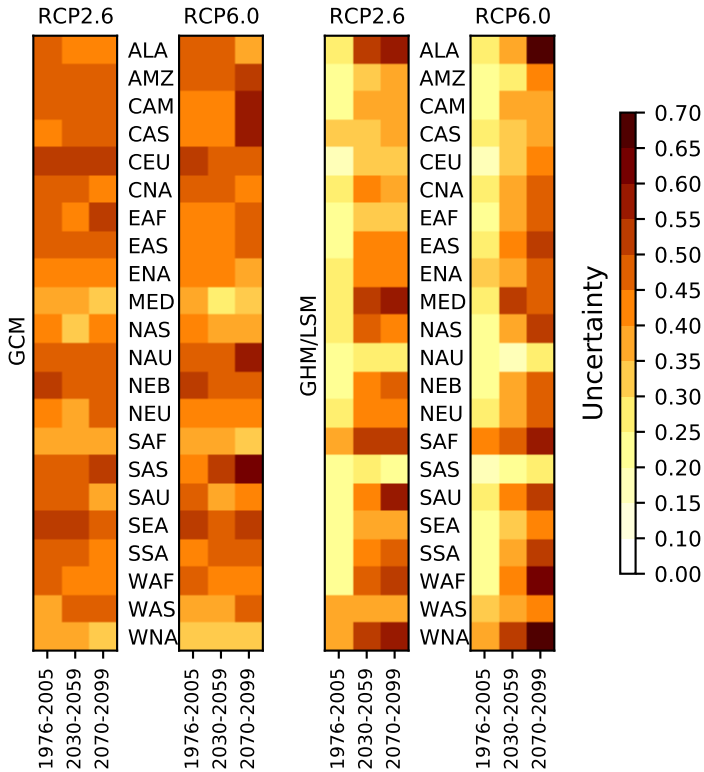


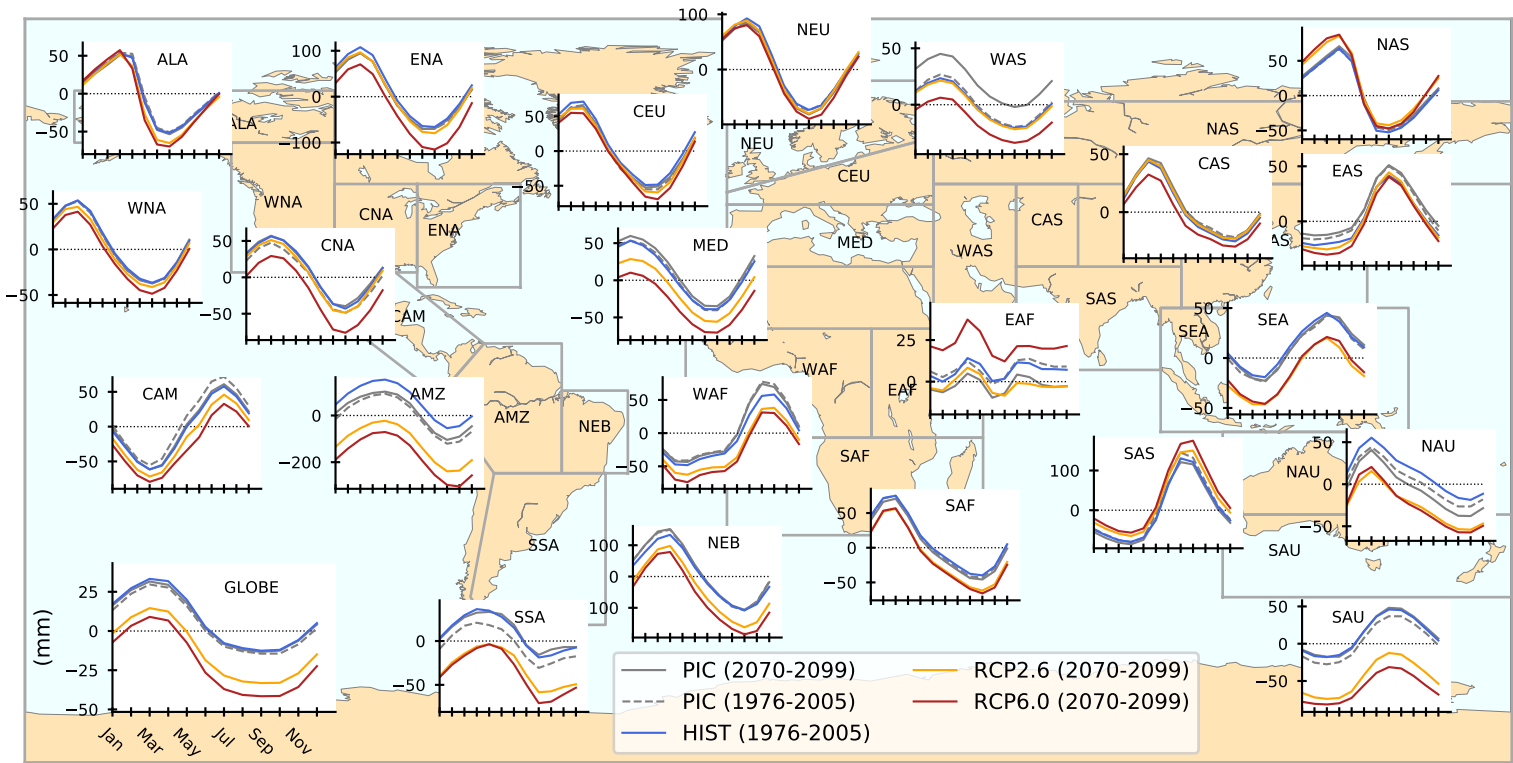
>75%
50%-75%
<50%

<-300 -200 -100 -50 -10 10 50 100 200 >300

(mm)

(mm)





— PIC (2070-2099) — RCP2.6 (2070-2099)
 - - - PIC (1976-2005) — RCP6.0 (2070-2099)
 — HIST (1976-2005)

